AFRL-RX-WP-TP-2009-4098

MODELING AND SIMULATION OF CAVITATION DURING HOT WORKING (PREPRINT)

P.D. Nicolaou, A.K. Ghosh, and S.L. Semiatin

Metals Branch
Metals, Ceramics and NDE Division

APRIL 2009

Approved for public release; distribution unlimited.

See additional restrictions described on inside pages

STINFO COPY

AIR FORCE RESEARCH LABORATORY
MATERIALS AND MANUFACTURING DIRECTORATE
WRIGHT-PATTERSON AIR FORCE BASE, OH 45433-7750
AIR FORCE MATERIEL COMMAND
UNITED STATES AIR FORCE

REPORT DOCUMENTATION PAGE

Form Approved
OMB No. 0704-0188

The public reporting burden for this collection of information is estimated to average 1 hour per response, including the time for reviewing instructions, searching existing data sources, searching existing data sources, gathering and maintaining the data needed, and completing and reviewing the collection of information. Send comments regarding this burden estimate or any other aspect of this collection of information, including suggestions for reducing this burden, to Department of Defense, Washington Headquarters Services, Directorate for Information Operations and Reports (0704-0188), 1215 Jefferson Davis Highway, Suite 1204, Arlington, VA 22202-4302. Respondents should be aware that notwithstanding any other provision of law, no person shall be subject to any penalty for failing to comply with a collection of information if it does not display a currently valid OMB control number. **PLEASE DO NOT RETURN YOUR FORM TO THE ABOVE ADDRESS**.

1. REPORT DATE *(DD-MM-YY)*	2. REPORT TYPE	3. DATES COVERED *(From - To)*
April 2009	Technical Paper Preprint	01 April 2009- 01 April 2009

4. TITLE AND SUBTITLE
MODELING AND SIMULATION OF CAVITATION DURING HOT WORKING (PREPRINT)

5a. CONTRACT NUMBER
In-house

5b. GRANT NUMBER

5c. PROGRAM ELEMENT NUMBER
62102F

6. AUTHOR(S)
P.D. Nicolaou, A.K. Ghosh, and S.L. Semiatin (AFRL/RXLMP)

5d. PROJECT NUMBER
4347

5e. TASK NUMBER
RG

5f. WORK UNIT NUMBER
M02R2000

7. PERFORMING ORGANIZATION NAME(S) AND ADDRESS(ES)

Metals Branch (RXLMP)
Metals, Ceramics and NDE Division
Materials and Manufacturing Directorate
Wright-Patterson Air Force Base, OH 45433-7750
Air Force Materiel Command, United States Air Force

8. PERFORMING ORGANIZATION REPORT NUMBER
AFRL-RX-WP-TP-2009-4098

9. SPONSORING/MONITORING AGENCY NAME(S) AND ADDRESS(ES)
Air Force Research Laboratory
Materials and Manufacturing Directorate
Wright-Patterson Air Force Base, OH 45433-7750
Air Force Materiel Command
United States Air Force

10. SPONSORING/MONITORING AGENCY ACRONYM(S)
AFRL/RXLMP

11. SPONSORING/MONITORING AGENCY REPORT NUMBER(S)
AFRL-RX-WP-TP-2009-4098

12. DISTRIBUTION/AVAILABILITY STATEMENT
Approved for public release; distribution unlimited.

13. SUPPLEMENTARY NOTES
To be submitted to Society ASM Handbook, Volume 22, Modeling and Simulation: Processing of Metallic Materials
PAO Case Number and clearance date: 88ABW-2009-1475, 10 April 2009.
This is a work of the U.S. Government and is not subject to copyright protection in the United States.

14. ABSTRACT
Many metallic materials develop internal cavities when subjected to large uniaxial or multiaxial tensile strains at elevated temperatures. These materials include conventional alloys of aluminum, titanium, copper, lead, and iron as well as emerging intermetallic materials such as titanium aluminide alloys [1-3]. For a given material, with a given microstructure, the extent of cavitation depends on the specific deformation conditions (e.g., strain rate, temperature, and stress state). In most cases, cavitation may lead to premature failure at levels of deformation far less than those at which flow-localization-controlled failure would occur. Cavitation is a very important phenomenon in hot working of materials because it may yield inferior properties in the final part let alone lead to premature failure during forming. Cavity formation usually comprises three distinct but simultaneously occurring stages, i.e. nucleation, growth, and coalescence. An important requirement for cavitation during deformation under either conventional hot-working (high-strain-rate) conditions or superplastic forming is the presence of a tensile stress.

15. SUBJECT TERMS
hot-working, uniaxial, multiaxial, cavitation

16. SECURITY CLASSIFICATION OF:			17. LIMITATION OF ABSTRACT:	18. NUMBER OF PAGES	19a. NAME OF RESPONSIBLE PERSON (Monitor)
a. REPORT	b. ABSTRACT	c. THIS PAGE			Sheldon L. Semiatin
Unclassified	Unclassified	Unclassified	SAR	68	19b. TELEPHONE NUMBER *(Include Area Code)* N/A

Standard Form 298 (Rev. 8-98)
Prescribed by ANSI Std. Z39-18

Modeling and Simulation of Cavitation during Hot Working

P.D. Nicolaou, A.K. Ghosh, and S.L. Semiatin
Air Force Research Laboratory, Materials and Manufacturing Directorate,
AFRL/RXLM, Wright-Patterson Air Force Base, OH 45433-7817

INTRODUCTION

Many metallic materials develop internal cavities when subjected to large uniaxial or multiaxial tensile strains at elevated temperatures. These materials include conventional alloys of aluminum, titanium, copper, lead, and iron as well as emerging intermetallic materials such as titanium aluminide alloys [1-3]. For a given material, with a given microstructure, the extent of cavitation depends on the specific deformation conditions (e.g., strain rate, temperature, and stress state). In most cases, cavitation may lead to premature failure at levels of deformation far less than those at which flow-localization-controlled failure would occur. Cavitation is a very important phenomenon in hot working of materials because it may yield inferior properties in the final part let alone lead to premature failure during forming.

Cavity formation usually comprises three distinct but simultaneously occurring stages, i.e. nucleation, growth, and coalescence. An important requirement for cavitation during deformation under either conventional hot-working (high-strain-rate) conditions or superplastic forming is the presence of a tensile stress. Under conditions of homogeneous compression, on the other hand, cavitation is typically not observed. In fact, cavities produced during tensile flow may often be closed during subsequent compressive flow. Similarly, it has been demonstrated that the superposition of a hydrostatic pressure during hot forming can reduce or even eliminate cavitation [4].

This article deals with the modeling and simulation of cavitation phenomena. It is divided into six sections. Experimental observations of cavitation are briefly summarized first. The next two sections review the modeling of cavity nucleation and

cavity growth; the former topic is treated more extensively in a companion article in this volume. The discussion of cavity growth focuses on both mesoscale and microscale models under uniaxial versus multiaxial tensile-stress conditions; mesoscale models incorporate the influence of local microstructure and texture on cavitation. Descriptions of cavity coalescence and shrinkage are summarized in the following two sections. The last part of this article deals with the simulation of the tension test to predict tensile ductility and to construct failure-mechanism maps.

CAVITATION OBSERVATIONS

Optical and SEM microscopy are the usual techniques applied to quantify cavity formation within metallic materials. Specifically, samples are sectioned along one or more directions and are prepared for metallograhic analysis. Low magnification optical microscopy permits a gross examination of the sample, while SEM investigation enables the observation of cavities in greater detail. Optical micrographs with magnifications between 50X and 200X are typically analyzed using commercial software packages (e.g. NIH, Image J) to obtain measurements of several important features of cavities, e.g. average radius, shape, angle with respect to the principal directions. Further analysis of such measurements is used to the determine the cavity area fraction, cavity volume, cavity density, and cavity shape [5, 6].

Higher magnification SEM analysis is often conducted in selected areas of a specimen in order to establish cavity nucleation sites, nucleation strain, onset of coalescence, coalescence mechanisms, etc. relative to microstructural features (triple points, second phase particles) that influence cavitation behavior. As an example, Figure 1a shows a typical optical micrograph used to determine the cavity features in Ti-6Al-4V following hot tension testing [5]; a corresponding high magnification SEM micrograph (Figure 1b) reveals the onset of coalescence of cavities.

Experimental measurements and observations of cavitation are summarized in Table 1 in which the broad test conditions and major conclusions related to cavitation behavior are summarized for a number of different alloys[7-18]. This list is not exhaustive, but provides an overview of the extent of the phenomenon. Observations for aluminum alloys are not included here inasmuch as they are discussed in the companion article by A.K. Ghosh.

As microscopic examinations reveal, cavitation comprises three distinct stages that usually occur simultaneously: nucleation, growth, and coalescence. The modeling of each of these stages is briefly described in the following sections.

MODELING OF CAVITY NUCLEATION

Nucleation represents the first stage of cavitation. Cavities nucleate by (i) the intersection of matrix slip bands with non-deformable second-phase particles or with grain boundaries, (ii) sliding along grain boundaries giving rise to stress concentrations at triple junctions that are not relaxed by diffusional transport, and/or (iii) the condensation of vacancies at grain boundaries.

Once a cavity is generated, the propensity for it to grow (or shrink) is determined from the local stress-equilibrium [19, 20]. Specifically, a cavity is stable when its size exceeds a critical radius r_c, which is given by the following relation:

$$r_c = 2\left(\gamma+\gamma_p-\gamma_i\right)\Big/\sigma \quad , \qquad (1)$$

in which γ, γ_p, and γ_i denote the surface energies of the cavity/void, the particle, and the particle-matrix interface; and σ is the applied stress. This criterion implies that flow hardening is required to continuously nucleate and grow cavities, which usually does not occur during conventional hot working or superplastic flow (except in cases of significant grain growth). The equation also leads to required stresses for initiation and early growth which are unrealistically high. Therefore, other methods based on

nucleation and growth from inhomogeneities/regions of high local stress triaxiality have been developed. For example, Ghosh, et al. [21] have developed a constrained-plasticity model in which nano-cavities nucleated by slip intersections with non-deformable second phase particles or grain boundaries grow due to stresses normal and/or parallel to the interface by local plasticity at the tip of a crack-like defect. In this case, the stress state is highly dilatational, and the early rate of growth is thus extremely rapid. The growth rate of a cavity decreases significantly as its size increases and becomes comparable to the microstructural feature that produces the constraint. Such models are described in more detail in the companion article on cavity nucleation.

MODELING OF CAVITY GROWTH

Cavity growth follows nucleation. Cavity-growth mechanisms can be classified into two broad categories: (i) diffusion-controlled growth and (ii) plasticity-controlled growth. Diffusional growth dominates when the cavity size is very small. As the cavity size increases, diffusional growth decreases very quickly, and plastic flow of the surrounding matrix becomes the controlling mechanism [19, 22]. An example of a cavity-growth-mechanism map, defining the different regimes, is shown in Figure 2.

Diffusion-controlled growth has been modeled [22-24] assuming spherical, widely spaced, and non-interacting cavities. The variation of the cavity radius r with effective strain $\bar{\varepsilon}$ is given by the following expression:

$$\frac{dr}{d\bar{\varepsilon}} = \frac{D\delta}{2kT\dot{\bar{\varepsilon}}}\Omega\frac{\bar{\sigma}}{r^2}\left(\frac{k_D}{3}+\frac{P}{\bar{\sigma}}+\frac{2\gamma}{r\bar{\sigma}}\right)\frac{1}{\ln(\lambda/2r)-3/4} \qquad (2)$$

Here, D is the diffusion coefficient, δ is the grain boundary thickness, k is Boltzmann's constant, Ω is the atomic volume, $\dot{\bar{\varepsilon}}$ is the effective strain rate, $\bar{\sigma}$ is the

effective stress, λ is the cavity spacing, P is the applied hydrostatic pressure, γ is surface energy, and k_D is a constant dependent on the geometry of the deformation.

The diffusional-growth mechanism is of limited engineering importance because the great majority of cavity growth occurs by a plasticity-controlled mechanism under the conventional hot-working conditions employed in industrial forming processes. In such cases, the cavity-growth rate depends on the deformation temperature, the strain rate, and the stress state. The remainder of this section, therefore, deals with the modeling of cavity growth under both *uniaxial* and *multiaxial* stress conditions.

Plasticity-Controlled Growth under Uniaxial-Tension Conditions

The plasticity-controlled growth of an isolated, non-interacting cavity during *uniaxial* tensile deformation is given by the following equation:

$$V=V_o\exp\left(\eta(\varepsilon-\varepsilon_o\right), \quad \text{or} \qquad r=r_o\exp\left(\frac{\eta}{3}\left(\varepsilon-\varepsilon_o\right)\right) \tag{3a}$$

or

$$\frac{dV}{d\varepsilon}=\eta V \qquad \frac{dr}{d\varepsilon}=\frac{\eta r}{3} \tag{3b}$$

In Equations (3), V and r are the cavity volume and radius respectively; V_o and r_o are the volume and radius of the cavity at a strain ε_o at which it becomes stable; ε denotes axial strain; and η is the individual cavity-growth rate parameter [18, 19, 25]. The cavity growth rate η is related to material parameters such as the strain rate sensitivity m, which itself is a function of deformation parameters (strain rate and temperature). For a planar array of spherical, non-interacting, grain-boundary cavities under *tensile* straining conditions, the following relation between η and m has been derived [26]:

$$\eta=1.5\left(\frac{m+1}{m}\right)\sinh\left[\frac{2}{3}\frac{(2-m)}{(2+m)}\right]. \tag{4}$$

This theoretical relationship has been found to describe experimental observations for a wide range of cavitating metals and alloys.

The measurement of the cavity-growth rate of an individual cavity is difficult because continuous nucleation and cavity coalescence takes place in parallel with growth. To overcome this problem, the cavity volume fraction C_v is measured; its variation with strain is described by a relationship similar to Equation (3), i.e.,

$$C_v = C_{v_o} \exp[\eta_{APP}(\varepsilon-\varepsilon_o)] , \qquad (5)$$

in which the *apparent* cavity-growth rate η_{APP} replaces the individual cavity growth rate η. The parameter η_{APP} is an "average" incorporating the growth of individual cavities, continuous cavity nucleation, and coalescence; η_{APP} is readily determined from semi-log plots of C_v versus ε [18, 27] (e.g., Figure 3). The data in Figure 3 correspond to a gamma titanium aluminide alloy tested in tension at a temperature of 1000°C and a strain rate of 10^{-4} s^{-1}. The slope of the fitted line equals η_{APP} [18].

Simulations of cavity growth with continuous nucleation have led to the delineation of the difference between η_{APP} and η. Typical simulation results (Figure 4) show the ratio η_{APP}/η as a function of the cavity nucleation rate N (defined as the number of cavities that initiate per unit volume and per unit strain) and the strain rate sensitivity. This ratio is close to unity when the cavity nucleation rate is low; however, it deviates from unity as N increases. In addition, it has been found that the dependence of η_{APP}/η on the strain rate sensitivity m is relatively weak [27].

The applicability of simple relations such as Equations (3) and (5) has been established by the modeling work conducted by Hancock [28] and Stowell [29].

Hancock Model. This plasticity-controlled growth analysis considers a single cylindrical hole in an incompressible viscous solid [28]. The model gives rise to an additional surface-tension term in Equation (3b), i.e., γ/r, in which γ is the surface

energy and is typically of the order of 1 J/m^2. The term γ/r may be viewed as a radial stress introduced on the surface of the cylindrical void. For such a void, the resulting equation is the following

$$\frac{dr}{d\varepsilon} = \frac{\eta}{3}\left(r - \frac{3\gamma}{2\sigma} \right) . \qquad (6)$$

The above expression reveals that the surface-tension term is negligible when the applied stresses are high, which is typically the case under hot-working conditions.

Stowell Model. The model of Stowell for plasticity-controlled cavity growth was developed for superplastic alloys. The analysis focuses on a cylindrical representative volume element with a diameter equal to the cavity spacing and a length equal to the grain diameter [29]. The model accounts for the increase in strain rate in the region where the cavity is present relative to that in the uncavitated region. An initial cavity elongates with strain, leading to the definition of an equivalent radius $r = (1/3)(a+2b)$, in which a and b denote the major and minor axes of the elliptical cavity, respectively. This approximation for the equivalent cavity radius becomes less accurate as the aspect ratio a:b increases. Assuming that the cavity volume (V) is proportional to r^3 and the cavity density (number of cavities per initial unit volume V_o) is N, the Stowell analysis leads to an expression similar to Equations (3).

Stowell's model has some limitations, mostly related to the assumptions that a fixed number of cavities grow from the beginning of the deformation and there is no interaction between neighboring cavities. In addition, it assumes the same law for the different directions of cavity growth.

Plasticity-Controlled Growth under Multiaxial Stress States

The stress state developed during industrial metalworking operations is usually multiaxial. To describe cavity growth, modifications must therefore be made to relations such as Equation (3a and b), which is strictly applicable for deformation

under uniaxial-tension conditions. For this purpose, the simplest approach consists of the application of a relation similar to Equations (3) in which the uniaxial-tension cavity-growth parameter η is replaced by a cavity-growth parameter for the complex stress state, i.e., η^{ts}, and the uniaxial strain ε is replaced by the effective strain $\bar{\varepsilon}$. A complex stress state is quantified by considering the stress ratio, $\sigma_M/\bar{\sigma}$, i.e., the ratio of the mean to effective stress. The cavity-growth rate-parameter η^{ts} is simply a function of $\sigma_M/\bar{\sigma}$, i.e.,

$$\frac{\eta^{ts}}{\eta}=F\left(\frac{\sigma_M}{\bar{\sigma}}\right). \qquad (7)$$

Thus, the multiaxial-stress analog of Equation (3a) is as follows:

$$r=r_o\exp\left[\frac{\eta^{ts}}{3}\left(\bar{\varepsilon}-\bar{\varepsilon}_o\right)\right] \text{ or } r=r_o\exp\left[\frac{\eta}{3}F\left(\frac{\sigma_M}{\bar{\sigma}}\right)\left(\bar{\varepsilon}-\bar{\varepsilon}_o\right)\right]. \qquad (8)$$

The function $F(\sigma_M/\bar{\sigma})$ is therefore required to describe cavity growth under multiaxial stress states. As described next, the function $F(\sigma_M/\bar{\sigma})$ has been determined using continuum mechanics approaches [30-33] as well as a semi-empirical methods [34].

McClintock Model. McClintock used a continuum approach to obtain equations that describe the growth of voids of different geometries under different stress conditions [32, 33, 35]. The initial focus was on the description of the growth of cylindrical voids in a linear hardening material subject to an axisymmetric stress state or in a rigid, non-hardening material under axisymmetric deformation conditions. This was followed by an assessment of the growth of voids within a moderately work-hardening material. The overall result was a law that describes the growth, within a shear band, of a cylindrical void of elliptical cross section in a linear-hardening matrix under arbitrary biaxial loading [36,37], i.e.,

$$\frac{1}{r}\frac{dr}{d\bar{\varepsilon}} = \frac{1}{2(1\text{-}n)}\sinh\left[(1\text{-}n)\frac{\sigma}{\tau}\right] \qquad (9)$$

in which τ is the shear stress within the shear band, σ is the normal stress across it, $\bar{\varepsilon}$ is the effective strain, and n is the strain-hardening exponent. A simple modification of Equation (9) provides an order of magnitude estimate for the growth of elliptical cavities by taking an average of the three principal stresses, i.e.

$$\frac{dR}{d\bar{\varepsilon}} = \left\{\frac{\alpha}{1\text{-}n}\sinh\left[(1\text{-}n)\frac{\sigma_M}{\tau_o}\right]\right\}R \qquad (10)$$

Here, R denotes the average of the three semi-axes of the cavity, α is a constant of the order of unity, and σ_M is the mean stress. This model shows that the void growth decreases as n increases. By analogy with Equation (3b), the term within the angular brackets in Equation (10) equals $\eta^{ts}/3$. The value of η^{ts} can be readily calculated from a relation derived by Rice and Tracey which is described next.

Rice-and-Tracey Model. A continuum-mechanics approach was also employed by Rice and Tracey [30] to describe the growth of a spherical cavity within a plastic, non-hardening material obeying the von Mises yield criterion. The strain field was assumed to comprise three contributions: (i) a uniform strain field due to plastic deformation of the matrix, (ii) a spherically-symmetric strain field resulting from the change of the cavity volume but involving no shape change, and (iii) a strain field (decaying at remote distances) which arises from changes of the void shape but not its volume. The analysis of Rice and Tracey revealed that the contribution of the change of the cavity shape to the strain is minimal; on the other hand, the other two factors had a much more potent effect. In fact, they showed that by neglecting the cavity-shape-change strain field, the error introduced was less than 1 pct. This

analysis led to the determination of the following dependence of η^{ts} on the stress ratio $\sigma_M/\bar{\sigma}$:

$$\eta^{ts} = 0.558 \sinh(3\sigma_M/2\bar{\sigma}) + 0.008\, \nu \cosh(3\sigma_M/2\bar{\sigma}), \qquad (11)$$

in which ν is a function of the principal strain rates, i.e., $\nu = -3\dot{\varepsilon}_2/(\dot{\varepsilon}_1 - \dot{\varepsilon}_3)$, with $\dot{\varepsilon}_1 \geq \dot{\varepsilon}_2 \geq \dot{\varepsilon}_3$.

Pilling-and-Ridley Model. An alternate, semi-empirical approach [34] has also been used to quantify the effect of the hydrostatic pressure P on the cavity growth rate η^{ts} for superplastic alloys which often exhibit extensive cavitation. The *empirical* relationship between η^{ts} and η is the following

$$\eta^{ts} = \eta\left(1 + 2\frac{P}{\bar{\sigma}}\right). \qquad (12)$$

P is taken to be negative if it is compressive and positive if it is tensile. Because $\sigma_M = P + \bar{\sigma}/3$, $P/\bar{\sigma} = \sigma_M/\bar{\sigma} - 1/3$, Equation (12) can then be rewritten in terms of the stress ratio, i.e.,

$$\eta^{ts} = \eta\left(\frac{1}{3} + 2\frac{\sigma_M}{\bar{\sigma}}\right) \qquad (13)$$

By combining Equations (8) and (13), therefore, the cavity size for a multiaxial stress state can be calculated.

Application of Models. The applicability of relations for η^{ts}/η such as Equations (10) to (13) [38] has been determined by comparing model predictions to experimental measurements. The collected measurements correspond to a variety of materials deformed under different stress states (e.g., equibiaxial tension, plane-strain tension, uniaxial tension of notched specimens, etc.) and processing conditions (i.e., temperature, strain rate). The experimental data fall within a broad scatter band (Figure 5). Model predictions are also shown in this figure. A comparison of the

scatter band and trend lines for the various equations indicates that none of the models provides precise predictions of the measurements. Nevertheless, the semi-empirical model described by Equation (13) does mirror the observed trend better than the others. In fact, the upper and lower limits of the experimental scatter band follow this relation (Equation (13)) multiplied by a factor Q equal to 0.75 or 1.25, respectively. Thus, the general correlation of cavity growth and stress state is described by the following relationship:

$$r=r_o \exp\left[\frac{\eta}{3} Q\left(\frac{1}{3}+2\frac{\sigma_M}{\bar{\sigma}}\right)\left(\bar{\varepsilon}-\bar{\varepsilon}_o\right)\right]. \qquad (14)$$

The usefulness of the correlation described by Equation (14) has been confirmed using two different sets of cavity-size measurements (Figure 6). The first set came from experiments involving a range of stress triaxialities developed during notched-tension testing of a titanium alloy [39], while the second focused on results from the equi-biaxial-tension testing of an aluminum alloy [40].

Measurements of the *average* diameter of cavities developed during notched-tension testing of Ti-6Al-4V (with a colony-alpha microstructure) at 815°C and a nominal strain rate of 0.1 s^{-1} [39] are plotted as a function of the stress ratio $\sigma_M/\bar{\sigma}$ in Figure 6a. The individual data points correspond to two different cavity-growth-strain-ranges, $\varepsilon-\varepsilon_o$. In addition, predictions for η = 6.5, values of the constant Q between 0.75 and 1.25, and the same levels of $\varepsilon-\varepsilon_o$ (i.e., ~0.14 and ~0.22) are also shown in the graph as shaded areas. It can be seen that the correlation embodied in Equation (14) bounds the experimental measurements well.

Measurements (data points) of the effective-strain dependence of the average diameter of cavities developed during the equi-biaxial-tension testing ($\sigma_M/\bar{\sigma}$ = 0.66) of a fine-grained, modified 5083 aluminum alloy at two different strain rates and a

temperature in the superplastic range are shown in Figure 6b [40]. Applying Equation (14) with Q= 0.75 and 1.25, a cavity-growth rate in uniaxial tension of $\eta = 3.2$, and an assumed nucleation strain ε_o of zero (solid lines), it is seen that model predictions bound the observations for this material as well.

Cavity-Growth Rate along the Principal Directions

In many cases, cavities do not grow as simple spheres whose radii increase with strain; rather, they grow as ellipsoidal voids. Hence, the use of a single cavity-growth parameter η (or η^{ts}) is not justified. In such cases, it is often useful to quantify the cavity-growth rate along each of the principal directions of the ellipsoidal cavity. In particular, the change of the size of a cavity along direction *i* may be described by the relation

$$L_i = L_{io} \exp(\eta_i \, \bar{\varepsilon}) \qquad (15)$$

in which L_i and η_i denote the size and cavity-growth-rate parameter along direction i.

As an example, directional cavity-growth has been observed during the hot torsion testing of Ti-6Al-4V [41]. The cavity-growth rates along the three principal specimen directions (z, r, θ) were determined by measuring the cavity sizes, L_z, L_r and L_θ via optical microscopy on the z-r and z-θ cross-sections. The measured average cavity lengths (L_z, L_r, and L_θ) as a function of effective strain (Figure 7) indicated that the cavity-growth parameter is indeed directional in nature $\{\eta\}$, i.e.,

$$\{\eta\} = \begin{pmatrix} \eta_z & & \\ & \eta_r & \\ & & \eta_\theta \end{pmatrix} = \begin{pmatrix} 0.05 & & \\ & 0.41 & \\ & & 0.46 \end{pmatrix}.$$

The *volumetric* cavity growth rate η equals the sum (trace) of the components of the above matrix, i.e.

$$\eta = \eta_z + \eta_r + \eta_\theta, \qquad \text{or} \qquad \eta = 0.92$$

The value $\eta = 0.92$ was found to be in broad agreement with the value of η if the cavities had been treated as spherical in shape.

Micromechanical Models of Plasticity-Controlled Growth

Classical plasticity-controlled models, such as those discussed above, neglect the effect of local texture and microstructure on cavity growth. As such, their principal use is for the prediction of the *average* cavity size and volume fraction developed during hot working or superplastic forming. However, it is the size of the *largest* cavities that play the most important role with respect to the properties and performance of a finished product. To this end, so-called micro-mechanical models that enable such predictions have been developed to fill this gap.

Micro-mechanical models [42, 43] focus on quantifying local stresses and the partitioning of strain between adjacent grains (or colonies in the case of a lamellar microstructure) due to differences in crystallographic orientation. The first analyses were developed for alpha/beta titanium alloys with a colony-alpha microstructure in which cavitation is quite severe. The plastic anisotropy of the alpha (hcp) phase leads to colonies with markedly higher or lower Taylor factors, which therefore behave differently during deformation.

Micro-mechanical cavity-growth models comprise three elements: (i) an analysis to estimate the approximate stress ratio within adjacent hard and soft grains or colonies, (ii) a self-consistent calculation for the partitioning of the macroscopic strain/strain rate to differently-oriented grains/colonies, and (iii) a plasticity-controlled model incorporating stress-state effects to estimate the actual cavity-growth kinetics (e.g., Equation (8)). The basic assumptions of these models are (i) the cavity formed at the boundary between a hard grain/colony and a soft grain/colony is small relative to the grain size and hence has little influence on the stresses and strains that are

developed in the absence of the cavity, and (ii) cavities grow into softer grains/colonies.

Uniaxial Tension. For uniaxial-tension deformation, the stress ratio ($\sigma_M/\bar{\sigma}$) controlling cavity growth *within the soft colony* is given by the following expression [42]:

$$\frac{\sigma_M}{\bar{\sigma}} = f_h \left[\frac{M_h}{M_s} \left(\frac{\dot{\bar{\varepsilon}}_h}{\dot{\bar{\varepsilon}}_s} \right)^m \left(\frac{\bar{\varepsilon}_h}{\bar{\varepsilon}_s} \right)^n - 1 \right] + \frac{1}{3} \qquad (16)$$

in which M, $\dot{\bar{\varepsilon}}$, $\bar{\varepsilon}$ denote the Taylor factor, strain rate, and strain of a hard (subscript h) or soft (subscript s) grain/colony, respectively; f_h is the volume fraction of the hard grains/colonies; and m and n denote the strain-rate sensitivity and the strain-hardening exponent, respectively. The partitioning of strain/strain rate between hard and soft grains/colonies, which is needed as input for both the stress-state (Equation (16)) and the cavity-growth (Equation (14) for Q=1) calculations, may be estimated from the self-consistent calculations [44], in which the relative strain rates are a function of the volume fraction of the hard grains/colonies and the ratio of strength coefficients/Taylor factors of the hard and soft grains/colonies. In Figure 8, model results of the ratio of the strain rate of higher-flow-stress grain/colony to the macroscopic (imposed) strain rate ($\dot{\varepsilon}_h/\dot{\varepsilon}_{tot}$) and the corresponding ratio for the lower-flow-stress grain/colony ($\dot{\varepsilon}_s/\dot{\varepsilon}_{tot}$) are given as a function of the ratio of the strength coefficients k_h/k_s and the volume different fraction f of the hard grain/colony. The strain rate in the higher-flow-stress (hard) phase is less than in the lower-flow-stress phase. The difference increases as either f decreases and/or k_h/k_s increases.

A typical application of the model for cavitation during hot tension of Ti-6Al-4V with a colony-apha microstructure is shown in Figure 9. Here, measured radii r (for cavities larger than 3 μm) (data points) are plotted as a function of the Taylor

factor ratio M_h/M_s. The solid lines represent model predictions; the strain at which each measurement corresponds is shown in the legend. The shaded bands correspond to a range of the fraction of the hard phase f_h between 0.4 and 0.8 (increasing from right to left, as shown by the arrow in the graph) and three different cavity-growth strain intervals, *i.e.*, ε-ε_o = 0.18, 0.35, and 0.55, in which ε_o denotes the cavity-nucleation strain. The line within the shaded area corresponds to $f_h = 0.6$. The model reveals that for a given M_h/M_s, the cavity radius increases as the fraction of the hard phase increases at the expense of the soft one, largely because the strain accommodated by the soft phase increases. However, the cavity radius has a stronger dependence on the strain at nucleation (ε-ε_o) than f_h. Overall, the experimental observations in Figure 9 are well bounded by the model predictions for a cavity-growth-strain range between 0.18 and 0.55, with the majority of cavity measurements lying close to the ε-ε_o = 0.18 condition[42].

Multiaxial Stress States. The principal aspects of the micro-mechanical analysis of cavity growth under a macroscopic *multiaxial* stress state also comprise estimates of the local stress state, the partitioning of strain/strain rate between hard and soft grains/colonies using a strain-partitioning model [44], and the application of the cavity-growth equation (Equation (14), for Q=1) to the soft colony.

The macroscopic stress state is assumed to comprise three principal stresses (e.g., axial (σ_z), radial (σ_r), and hoop (σ_θ) for axisymmetric deformation), which can be determined from finite-element-method (FEM) analysis. The microscopic *local* stresses in the hard and soft grains/colonies are determined by taking into account the yield functions of the hard and soft colonies and the relevant local-equilibrium equations. For a material obeying the von Mises yield criterion, the yield-function relationships are:

$$\bar{\sigma}_h = \frac{1}{\sqrt{2}}\left\{\left(\sigma_{\theta_h} - \sigma_{z_h}\right)^2 + \left(\sigma_{z_h} - \sigma_{r_h}\right)^2 + \left(\sigma_{r_h} - \sigma_{\theta_h}\right)^2\right\} \quad (17)$$

$$\bar{\sigma}_s = \frac{1}{\sqrt{2}}\left\{\left(\sigma_{\theta_s} - \sigma_{z_s}\right)^2 + \left(\sigma_{z_s} - \sigma_{r_s}\right)^2 + \left(\sigma_{r_s} - \sigma_{\theta_s}\right)^2\right\} \quad (18)$$

The subscripts θ, r, and z refer to the specific *principal* stress components; the subscripts h and s refer to the hard and soft colonies, respectively; and $\bar{\sigma}_h$ and $\bar{\sigma}_s$ denote the flow stress of the soft and hard colonies, respectively.

The macroscopic axial (σ_z^{mac}) and radial (σ_r^{mac}) stresses which are determined from FEM analysis are each assumed to be a rule-of-mixtures average of the corresponding stress components in the hard and soft colonies, thus satisfying the load equilibrium considerations, i.e.,

$$\sigma_z^{mac} = f_h \sigma_{z_h} + (1 - f_h)\sigma_{z_s} \quad (19)$$

$$\sigma_r^{mac} = f_h \sigma_{r_h} + (1 - f_h)\sigma_{r_s} \quad (20)$$

Furthermore, the hoop stress is usually taken to be essentially the same in the soft and hard grains/colonies and is equal to the macroscopic (FEM) stress σ_θ^{mac}, i.e.,

$$\sigma_\theta^{mac} = \sigma_{\theta_h} = \sigma_{\theta_s} \quad (21)$$

If the flow stresses of the hard ($\bar{\sigma}_h$) and the soft ($\bar{\sigma}_s$) colonies are known, the axial and radial stresses in each colony can be determined by solving Equations (17) to (21). More typically, $\bar{\sigma}_s$ and $\bar{\sigma}_h$ are determined by applying the self-consistent model to estimate the strain rates and hence the flow stresses in the hard and soft colonies [43, 44].

Having determined the stress components, the stress ratio $\sigma_M/\bar{\sigma}$ in both the hard and soft colonies can be calculated. Because the soft colony undergoes more strain than the hard colony, micromechanical cavity-growth calculations are typically

based on the strain in the soft colony and the value of η^{ts} corresponding to its stress ratio. The values of the strain and η^{ts} in the softer colony are then used to estimate the size of the largest colonies per Equation (8).

The micromechanical model for the size of the largest cavities developed under a state of multiaxial stress has been validated via observations for the hot pancake forging of cylindrical Ti-6Al-4V preforms with a colony-alpha structure [43] (Figure 10). Typical calculations of the stress ratio ($\sigma_M/\bar{\sigma}$) developed *within* the hard and soft colonies at the equatorial free surface reveal that the stress ratio in the softer colony is very sensitive to the Taylor factor ratio M_h/M_s, whereas it exhibits a much weaker dependence on M_h/M_s and has smaller values for the harder colonies. Model predictions for the size of the largest cavities (based on the calculated stress ratio, the corresponding values of η^{ts}, and the strain in the softer colony from the strain-partitioning model) are compared to measured radii of the large cavities (data points) as a function of distance form the free surface in Figure 11. This comparison shows that the model mimics the observed behavior with the best fit obtained for M_h/M_s between 1.5 and 3.

MODELING OF CAVITY COALESCENCE

Cavity coalescence refers to the stage at which voids link together leading to final fracture. In most models, cavity coalescence/linkage is assumed to occur between first and second nearest-neighbor cavities only. If it is postulated that there is no nucleation of new cavities, then two coalescence mechanisms are possible [45-47], viz.,

(i) Impingement: This mechanism refers to the exhaustion of the ligament between the two cavities. As two cavities grow, the ligament between them is

reduced until the outer surfaces of the cavities come into contact. This condition is described by the following relation:

$$s - (r_i + r_j) = 0 \ , \qquad (22)$$

in which s denotes the center-to-center cavity spacing, and r_i and r_j the instantaneous radii of cavities "i" and "j", respectively. It is important to note that a small initial inter-cavity spacing does not necessarily imply that coalescence will occur, because the horizontal *and* vertical spacing as well as the cavity-growth rate are both important.

(ii) Internal necking: Rupture of matrix material between two cavities occurs as a result of plastic instability and flow localization, much as though the cavities and matrix between them form a microscopic tension specimen. Various criteria for describing coalescence *via* such an internal-necking process have been based on (1) a critical matrix-ligament strain, ε_{cr}, (2) a critical stress, or (3) a critical void volume fraction. The first criterion is the one applied in most cases.

The critical matrix ligament strain ε_{cr}, depends on the initial cavity spacing and the individual cavity growth rate η. This strain can be determined by considering the deformation of a "microspecimen" containing two cavities along its mid-plane, which act like a geometric defect. Details of such simulations are given below in the section on tensile ductility. Here, typical results for such a mechanism are summarized in terms of the critical strain as a function of the center-to-center cavity distance and the cavity growth rate, η (Figure 12) [47]; the critical strain increases as d increases and/or as η decreases.

Cavity coalescence may also be regarded as a process which in effect increases the *average* cavity growth rate. In particular, the effect of pairwise

coalescence on the average cavity growth rate $d\bar{r}/d\bar{\varepsilon}$ can be estimated from the following equation [48]:

$$\frac{d\bar{r}}{d\bar{\varepsilon}} = \frac{8C_v\Phi\eta\left(0.13r - 0.37\left(dr/d\bar{\varepsilon}\right)_i \delta\bar{\varepsilon}\right) + \left(dr/d\bar{\varepsilon}\right)_i}{1 - 4C_v\Phi\eta\delta\bar{\varepsilon}} \quad , \qquad (23)$$

in which C_v is the instantaneous volume fraction of cavities, η is the uniaxial-tension cavity-growth parameter (Equation (3)), $\delta\bar{\varepsilon}$ $(=d\bar{\varepsilon})$ is a small increment of strain, $(dr/d\bar{\varepsilon})_i$ is the rate of growth per unit strain of an isolated cavity $(= \eta r/3$ from Equation (3)), and Φ is given by:

$$\Phi = (1 + \eta\ \bar{\varepsilon}\,\delta\varepsilon/3 + (\eta\ \delta\ \bar{\varepsilon})^2/27)\,. \qquad (24)$$

Equation (23) can be easily applied to predict average cavity size by a simple spreadsheet analysis, in which strain is the independent variable and the average cavity size the dependent variable. An example of the application of Equation (23) is shown in Figure 13 for a material with an individual cavity growth rate (η) equal to 3. The cavity size for coalescence or no coalescence along with the corresponding cavity volume fraction are shown in this figure. These results show that the effect of coalescence on the average cavity radius becomes noticeable when the cavity volume fraction exceeds ~7 pct.

In spite of prior research in this area, coalescence mechanisms are still not fully understood due to the experimental challenge in obtaining reliable data for the population of cavities during the process. These difficulties are associated primarily with the complex shapes of cavities. However, the recent application of novel experimental techniques has partially overcome such challenges. For example, Dupuy and Blandin [22] and Martin, et al. [49] have conducted X-ray micro-tomography to obtain 3D images of cavity populations in a non-destructive manner (Figure 14). From this work, a coalescence or interlinkage parameter (IP) has been introduced.

This parameter is the ratio of the volume of the largest cavity to the total volume of cavities in the specific region investigated. The micro-tomography results suggest that coalescence occurs over relatively large domains of strain and cavity volume fractions [22, 49]. For example, Figure 15 shows the variation of IP with the cavity volume fraction (which itself increases with strain) for aluminum alloy 5083 tested at 525°C and a strain rate 10^{-4} s^{-1}. The value of IP is relatively low (< 0.05) for a cavity volume fraction ≤5% (corresponding to a strain of ~1.2), and then it increases sharply.

MODELING OF CAVITY SHRINKAGE

Cavities which nucleate and grow under a tensile state of stress may be reduced in size during a change in strain path during which the stress state becomes compressive. A micro-mechanical model that describes cavity-shrinkage kinetics has been developed and applied [50]. In this approach, the stresses developed within the soft grains/colonies during a strain-path change which gives rise to *compressive* triaxiality are estimated in the same way as in the case of open-die forging, i.e., by applying the yield conditions and load-equilibrium equations. To estimate the strain-rate components and thus the densification rate $\dot{\rho}=\dot{\varepsilon}_{11}+\dot{\varepsilon}_{22}+\dot{\varepsilon}_{33}$, the stresses are inserted into a model for the consolidation of porous media [51], i.e.,

$$\dot{\varepsilon}_{ij}=\left(\frac{K(\rho)j^2\dot{\bar{\varepsilon}}}{\bar{\sigma}}\right)\left[(1+\nu)\sigma'_{ij}+(1-2\nu)\sigma_M\delta_{ij}\right] \qquad (25)$$

in which $\dot{\varepsilon}_{ij}$ denotes the strain rate tensor, σ'_{ij} is the deviatoric stress tensor, σ_M the mean stress, $\bar{\sigma}$ is the effective stress, ν is the Poisson's ratio of the porous body, and ϕ is the stress intensification factor, and δ_{ij} is the Kronecker delta. The function $K(\rho)$ is associated with the relative density ρ; it is commonly assumed to be equal to ρ when the latter is greater than 90 pct.

The applicability of Equation (25) to model cavity shrinkage has been demonstrated for Ti-6Al-4V with a colony-alpha microstructure subjected to torsion followed by reversed torsion or uniaxial compression (Figure 16). Cavity-shrinkage predictions [50, 51] showed good agreement with such observations (Figure 17a and b). The more rapid closure kinetics during compression compared to reversed torsion (as shown in the micrographs in Figure 16 were quantified correctly. Such results were explained on the basis of the higher levels of compressive stress triaxiality in compression compared to those in reversed torsion, the orientation of cavities in torsion relative to the applied stresses, and dynamic spheroidization of the microstructure which affected the stress triaxility in torsion to a greater extent than in compression.

MODELING AND SIMULATION APPROACHES TO PREDICT TENSILE DUCTILITY AND DEVELOP FAILURE MODE MAPS

Cavitation may lead to premature failure and thus to a significant reduction in the tensile ductility or forming limit relative to that in materials that do not cavitate but fail instead by strain localization prior to fracture [52] . For a given value of the strain rate sensitivity (m), the decrease in elongation for fracture-controlled failures due to cavitation depends on the rates of cavity nucleation and growth, the cavity shape and size distribution, and the spatial distribution of the cavities.

Early models of the effect of cavitation on failure (e.g., Reference 53) focused only on the effect of cavity generation on flow stability in uniaxial tension. In these approaches, it was assumed that that all cavities were spherical and uniformly distributed across a given cross-section; triaxiality and stress concentration effects were neglected. The models postulated that cavitation increases the three dimensions of the specimen (length, width, thickness) in proportion to the level of cavitation. Key results indicated that the progress of cavity generation renders deformation less stable

by reducing the effective values of both the strain-hardening exponent (which impacts the uniform elongation primarily) and the strain rate sensitivity (which affects the rate of flow localization following the onset of instability.)

More recent models quantify the effect of cavitation on tensile ductility in more detail. These approaches include those which do not or do incorporate the effect of stress triaxiality in the neck on cavitation.

Long-Wavelength Models

Long-wavelength models of the tension test seek to quantify cavitation and flow localization behavior by assuming that the neck developed after the onset of instability has a very long wavelength, and thus the stress triaxiality due to necking can be neglected [54, 55]. In such situations, cavitation and strain localization behavior are quantified by determining the relative deformation of two material slices (one with an initial defect of some sort) via a simple load-equilibrium approach. In particular, the analysis is based on the principle that the load (= axial stress multiplied by the cross-sectional area) transmitted through the two slices representing the specimen is constant. For a *non-cavitating* material, deformed in uniaxial tension, the following equilibrium expression is obtained:

$$\exp(-\varepsilon/m)\varepsilon^{n/m}d\varepsilon=\left(1-F\right)^{1/m}\exp\left(-\varepsilon_N/m\right)\varepsilon_N d\varepsilon_N \qquad (26)$$

In Equation (26), the subscript N refers to an initial geometric defect, F; $F=\left(A_o-A_{oN}\right)/A_o$, in which A_o and A_{oN} denote the area of the uniform and defected slice of the specimen.

For a *cavitating* material, cavity growth decreases the effective cross-sectional area of the specimen. Combining Equations (5) and (26) and assuming a uniform distribution of cavities, the following equilibrium relation is obtained in long-wavelength two-slice models:

$$\exp(-\varepsilon/m)\varepsilon^{n/m}\left\{1-C_{vo}\exp\left[\eta_{APP}\left(\varepsilon-\varepsilon_o\right)\right]\right\}^{1/m}d\varepsilon= \\ \left(1\text{-}F\right)^{1/m}\exp\left(-\varepsilon_N/m\right)\varepsilon_N\left\{1-C_{vo}\exp\left[\eta_{APP}\left(\varepsilon_N-\varepsilon_o\right)\right]\right\}^{1/m}d\varepsilon_N \quad (27)$$

Lian and Suery [56] were the first to develop and apply an expression of the form of Equation (27). In their simulations, they assumed an initial cavity volume fraction (C_{vo}) between 10^{-3} and 10^{-4}. Cavitation failure was assumed to occur when the cavity volume fraction in the defect region reached 30 pct. From such analyses, maps showing the failure mode as a function of m and η can be derived. The maps are divided into three regimes: (i) a regime in which the material fails by flow localization/necking, (ii) a regime in which cavity growth dominates and leads to failure without pronounced flow localization, and (iii) and an intermediate mixed-mode regime in which both cavitation and necking contribute to failure. Model predictions typically show good first-order agreement with observations in the literature despite the fact that a precise description of cavity nucleation and coalescence is not included in the analysis.

Macroscopic, two-slice, long-wavelength model can be extended to establish the effect of superimposed hydrostatic pressure on the failure mode [57]. For given values of m and η, the predicted failure mode changes when the superimposed pressure is greater than a certain value. It has been found that materials which fail without neck formation under zero-pressure conditions do indeed undergo flow localization prior to fracture when high pressures that suppress cavity growth are imposed.

Analogous to the macroscopic, long-wavelength analysis to determine ductility and failure mode, *microscopic* load-equilibrium approaches have been developed to investigate the internal necking and failure of the ligament between two cavities and hence the cavity-coalescence phenomenon. These latter techniques

typically rely on a representative micro-specimen (lying within the material) with a uniform rectangular cavity array (Figure 18). In this case, a load-equilibrium analysis, such as that developed by Zaki [58], can be used to treat the straining process within the uniform and necked/defect portions of the specimen, the latter representing the ligament between two cavities. The load-equilibrium equation is:

$$\varepsilon_u^{n/m} d\varepsilon_u = \varepsilon_i^{n/m} \left\{1 - r_o \exp\left[(\eta/3)\varepsilon_i\right]\right\}^{2/m} d\varepsilon_i \qquad (28)$$

in which n is the strain hardening exponent, m is the strain rate sensitivity, ε_u is the strain in the uniform region, and ε_i the strain in the defect portion of the specimen. Failure is assumed to occur when the ratio $\varepsilon_i/\varepsilon_u$ tends toward infinity. It has been found that the strain rate sensitivity strongly affects the total strain when the individual cavity growth rate is low (< 3).

Macroscopic Load-Equilibrium Approach with Stress Triaxiality

A load-equilibrium approach including the influence of stress triaxiality developed within the neck on flow localization and failure during tension testing provides more physically realistic estimates of ductility and failure mode than long-wavelength models for both cavitating and non-cavitating materials [59, 60]. For a sheet or round-bar tension test, the formulation is based on (i) a discretized sample geometry rather than merely two slices (e.g., Figure 19), (ii) a description of the material flow (stress-strain) behavior, (iii) an appropriate load-equilibrium equation (to describe the relation between the strain rate in each slice to that in the middle slice), and (iv) a specified boundary condition (e.g., constant crosshead velocity).

For a cavity free material flow behavior, the simple engineering power-law formulation is often used, i.e.:

$$\bar{\sigma} = K\bar{\varepsilon}^n \dot{\bar{\varepsilon}}^m \qquad (29)$$

in which $\bar{\sigma}, \bar{\varepsilon}$, and $\dot{\bar{\varepsilon}}$ denote the effective stress, effective strain, and effective strain rate, respectively, K, n, and m represent the strength coefficient, strain-hardening exponent, and the strain-rate-sensitivity index, respectively.

At any instant of deformation, the axial load is the same in each element in order to maintain equilibrium. When cavitation occurs, the load bearing area A_{lb} differs from the apparent, or macroscopic, area A_m. Assuming spherical and uniformly spaced cavities, the relationship between the two quantities (denoting the initial (uncavitated) area as A_o^{sp}) is:

$$A_m = A_{lb} \Big/ \left(1-C_v\right)^{2/3}, \quad \text{and } A_{lb} = A_o^{sp} \exp\left(-\bar{\varepsilon}\right): \tag{30}$$

The load borne by each slice is equal to the product of its load bearing cross-sectional area and axial stress; the axial stress is equal to the flow stress corrected for stress triaxiality due to necking and evaluated at a strain rate corresponding to that which the material elements experience. The load equilibrium condition is thus described by:

$$\bar{\sigma}_i A_{lb}^i / F_T^i = \bar{\sigma}_j A_{lb}^j / F_T^j \tag{31}$$

in which the subscripts and/or superscripts i and j denote the corresponding parameters for elements i and j, respectively; F_T represents the triaxiality factor; and A_{lb} is the load bearing area. The triaxiality factor at the symmetry plane of the neck (as well as away from this plane, at least to a first order) is given by the following equations for round-bar (F_T^r) and sheet (F_T^s) specimen geometries:

$$F_T^r = \left\{ \left[1+\left(2\frac{U}{w} \right) \right] \ln \left[1+\left(\frac{w}{2U} \right) \right] \right\}^{-1} \tag{32a}$$

$$F_T^s = \left\{ \left(1+2\frac{U}{w} \right)^{1/2} \times \ln \left[1+\frac{w}{U}+\left(\frac{2w}{U} \right)^{1/2} \left(1+\frac{w}{2U} \right)^{1/2} \right] -1 \right\}^{-1} \tag{32b}$$

in which w represents the specimen half diameter or half width, and U is the profile radius of the neck[61].

The matrix strain rate $\bar{\dot{\varepsilon}}$, i.e. the strain rate of the cavity free material can also be related to the macroscopic sample strain rate $\dot{\bar{\varepsilon}}_m$ (measured from the rate of change of the specimen's dimensions). Using power dissipation arguments, the relation between the two strain rates is the following [57]:

$$\bar{\dot{\varepsilon}}=\left(1/\varphi\ \rho\right)\ \dot{\bar{\varepsilon}}_m\ , \qquad (33)$$

in which ρ is the relative density of the specimen (ρ= 1-C_v), C_v is the cavity volume fraction, and φ is the stress intensification factor, which for spherical and uniformly distributed cavities is given by $\varphi=1/\rho^{2/3}$.

Equations (29) to (33) can be used to simulate the isothermal, hot tension test of a cavitating material. Briefly, such simulations comprise the following steps:

Step 1: Specify the initial specimen geometry (width, thickness, length, and initial cavity volume fraction in each element) as well as the overall nominal (or true) strain rate for the tension test. Calculate F_T for each element using Equations (32).

Step 2: Based on the geometry and local cavity volume fraction, determine the initial strain rate distribution for each element in the specimen relative to that in the central (reference) element using Equation (31). Determine absolute values of strain rate using the boundary condition. Here, use is made of the material constitutive relation (Equation (29) with the strain rate from Equation (33)).

Step 3: Impose an increment of deformation (based on the strain rate calculated in Step 2) and cavitation (based on Equation (5)) for each element, and determine the new specimen geometry, F_T distribution, and local cavity volume fractions.

Step 4: Calculate the engineering stress and strain.

Step 5: Calculate a new strain rate distribution using Equation (31) as in Step 2.

Step 6: Repeat Steps 3 to 5 until failure

Simulation outputs include predictions of engineering stress-strain curves and the total elongation at failure. For example, typical predictions of tensile elongation for sheet materials which exhibit strain-rate hardening [60] (with a rate-sensitivity index of m) and no strain hardening are shown in Figure 20. The figure illustrates the increase of ductility with increasing m and decreasing η_{APP}. In addition, by incorporating a fracture criterion (e.g., fracture occurs when the cavity volume fraction in an element reaches 30 pct.), the competition between flow-localization and cavitation-controlled failure can be quantified and used to construct maps showing the failure mode as a function of m and η_{APP}. For example, a failure-mode map for non-strain hardening materials is plotted in Figure 21 [60]. For deformation under superplastic conditions ($m > 0.3$) and $\eta_{APP} > 2$, the map shows that failure is fracture/cavitation controlled. On the other hand, flow-localization-controlled failure is seen to predominate only for small values of the apparent cavity growth rate.

Failure observations for several titanium aluminide alloys (Figure 22) illustrate the types of behavior that can be modeled by this approach. For example, a flow-localization type of failure (Figure 22a) has been observed for the orthorhombic titanium aluminide alloy Ti-21Al-22Nb deformed at 980°C and a nominal strain rate of 1.6×10^{-3} s^{-1} [63]. On the other hand, the gamma titanium aluminide alloy Ti-45.5Al-2Cr-2Nb exhibits fracture prior to flow localization during tension testing at 1200°C and a nominal strain rate of 10^{-3} s^{-1} (Figure 22b) [64]. The values of m, η_{APP} and the corresponding failure modes that pertain to these (and similar) experimental

observations are cross plotted in Figure 21. The solid data points represent fracture-controlled failures, while the open ones flow-localization-controlled failures. The predicted failure modes based on the values of m and η_{APP} show good agreement with the observations.

Hybrid Macro-Micro Modeling

The various features of the macroscopic load-equilibrium model with stress triaxiality and the micro-specimen (cavity-coalescence) model described in the previous two sections can be combined to develop a hybrid macro-micro model for the tensile behavior of cavitating materials [47]. In such a hybrid model, the critical strain (ε_{cr}) for inter-cavity ligament rupture due to internal necking at a micro-scale are determined from simulations of the deformation of a micro-tension specimen [58]; these simulations provide ε_{cr} as a function of cavity spacing d and material parameters such as the strain-rate-sensitivity index (m) and the cavity growth rate (η). The steps of this hybrid model are similar to the ones of the macroscopic load equilibrium approach. The major difference lies in the fact that the load bearing area is determined from (i) the macroscopic area of each slice of the specimen and (ii) the projection of the void area in the horizontal plane of this slice. Therefore, the load-bearing area is not necessarily constant within a particular slice at a given level of tensile elongation. Rather, it is smallest in regions heavily populated with cavities or in regions in which extensive coalescence has occurred. In addition, the location of the minimum load-bearing area within a given slice is not the same at two different levels of deformation because of cavity coalescence. For example, the minimum load-bearing area may have been located in a region with the highest local cavity density during an initial deformation stage. However, because not all cavity coalescences take place simultaneously, but rather progress with strain, the minimum load-bearing area

at a later stage of deformation may have then been located where the maximum number of coalescences had occurred.

Model predictions of engineering stress-strain curves from both a macroscopic model and a hybrid macro-micro model are presented in Figure 23 for a non-strain-hardening material assuming a range of individual cavity growth rates η and a constant (i.e., no new nucleation) cavity density of N = 100 cav/mm^2. The hybrid model predicts that flow localization occurs earlier during the deformation/cavitation process compared to the macroscopic model. Furthermore, flow localization appears to be more predominant in the hybrid model for the cavity-growth rates η considered. In fact, for $\eta = 2$, the shape of the engineering stress-strain curve suggests noticeable flow localization for the hybrid model, but a fracture-controlled failure mode for the macroscopic model. The predicted trends are similar for higher initial cavity densities as well. Such behavior can be ascribed to the fact that the hybrid analysis considers randomly-, rather than uniformly-, dispersed cavities within the specimen, and the cavity population and coalescence in a particular area affect the load-bearing area [47]. Therefore, the load-bearing area is constant within a slice for the macroscopic model. On the other hand, this area varies even within the same slice for the hybrid model, inasmuch as it depends on the *local cavity concentration* and/or coalescences which occur in a particular (local) region of the slice. As a result, as deformation proceeds, the load-bearing area is lower in the hybrid model. Hence, the load-bearing area decreases more rapidly with strain in the hybrid model, and the engineering stress is lower and decreases more rapidly with engineering strain.

SUMMARY

The parameters that govern the cavitation process during the hot working of metals have been summarized. Models of plasticity-controlled cavity growth, both for

uniaxial and complex (multiaxial) states of stress, are relatively advanced compared to those for the nucleation and coalescence of cavities. In many cases, mesoscale models of plasticity-controlled growth can provide reasonable estimates of the average cavity size. Microscale analyses enable the prediction of the size of the largest cavities by taking into account local microstructure and texture effects. Nevertheless, models of cavity nucleation and coalescence are important with respect to predicting overall tensile ductility. Last, models are being developed to treat the shrinkage of cavities that result from changes in stress state/strain path during complex industrial hot-working processes.

REFERENCES

1. M.I. Ahmed and T.G. Langdon. *Metall. Trans. A*, Vol. 8A, 1977, pp. 1832-1833.

2. S.L. Semiatin, V. Sheetharaman, A.K. Ghosh, E.B. Shell, and P.N. Fagan, *Mater. Sci. Eng. A*, Vol. A256, 1998, pp. 92-110.

3. C.C. Bampton and J.W. Edington, *J. Eng. Mater. Tech.*, Vol. 105, 1983, pp. 55-60.

4. J. Pilling and N. Ridley, , Superplasticity in Aerospace, H.C. Heikkenen and T.R. McNelly, TMS, Warrendale, PA, 1988, pp. 183-197.

5. P.D. Nicolaou, R.L. Goetz, J.D. Miller, and S.L. Semiatin, *Metall. Mater. Trans. A*, Vol. 34A, 2003, pp. 2397-2400.

6. P.D. Nicolaou and S.L. Semiatin, *Acta Mater.*, Vol. 51, 2003, pp. 613-623.

7. C.W. Humphries and N. Ridley, *J. Mater. Sci.*, Vol. 13, 1978, pp. 2477-2482.

8. C.H. Caceres and D.S. Wilkinson, *Acta Metall.*, Vol. 32, 1984, pp. 423-434.

9. C.H. Caceres and D.S. Wilkinson, *Scripta Metall.*, Vol. 16, 1982, pp. 1363-1365.

10. J. Belzunce and M. Suery, *Acta Metall.*, Vol. 31, 1983, pp. 1497-1504.

11. T. Chandra, J.J. Jonas, and D.M.R. Taplin, *J. Mater. Sci.*, Vol. 13, 1978, pp. 2380-2384.

12. A.H. Chokshi, *Metall. Trans. A*, Vol. 18A, 1987, pp. 63-67.

13. S. Sagat and D.M.R. Taplin, *Acta Metall.*, Vol. 24, 1976, pp. 307-315.

14. D.W. Livesey and N. Ridley, *J. Mater. Sci.*, Vol. 13, 1978, pp. 825-832.

15. D.W. Livesey and N. Ridley, *Metall. Trans. A*, Vol. 13A, 1982, pp. 1619-1626.

16. M.M.I. Ahmed, F.A. Mohamed, and T.G. Langdon, *J. Mater. Sci.*, Vol. 14, 1979, pp. 2913-2918.

17. B-N Kim, K. Hiraga, Y. Sakka, and B-K Jang, *Scripta Mater.*, Vol. 45, 2001, pp. 61-67.

18. C.M. Lombard, A.K. Ghosh and S.L. Semiatin, *Metall. Mater. Trans. A.*, Vol. 32A, 2001, pp. 2769-2779.

19. B.P. Kashyap and A.K. Mukherjee, *Res Mechanica*, Vol. 17, 1986, pp. 293-355.

20. G.H. Edward and M.F. Ashby, *Acta Metall.*, Vol. 27, 1979, pp. 1505-1518.

21. A.K. Ghosh, D-H. Bae, and S.L. Semiatin, *Mater. Sci. Forum*, Vols. 304-306, 1999, pp. 609-616.

22. L. Dupuy and J.-J. Blandin, *Acta Mater.*, Vol. 50, 2002, pp. 3251-3264.

23. M.V. Speight and W. Beere, *Metal Sci.*, Vol. 9, 1975, pp. 190-191.

24. A. Needleman and J.R. Rice, *Acta Metall.*, Vol. 28, 1980, pp. 1315-1332.

25. A.K. Chokshi, *J. Mater. Sci.*, Vol. 21, 1986, pp. 2073-2082.

26. A.C.F. Cocks and M.F. Ashby, *Metal Sci.*, Vol. 16, 1982, pp. 465-478.

27. P.D. Nicolaou, S.L. Semiatin, and A.K. Ghosh, *Metall. Mater. Trans. A*, Vol. 31A, 2000, pp. 1425-1434.

28. J.W. Hancock, *Metal Sci.*, 1976, pp. 319-325.

29. M. J. Stowell, *Metal Sci.*, 1980, pp. 267-272.

30. J.R. Rice and D.M. Tracey, *J. Mech. Phys. Solids*, Vol. 17, 1969, pp. 200-217.

31. P.F. Thomason: *Ductile Fracture of Metals*, Pergamon Press, 1990.

32. F. A. McClintock, *Ductility*, ASM, Metals Park, OH, 1968, pp. 255-277.

33. F. A. McClintock, S.M. Kaplan, and C.A. Berg, *Int. J. Fract. Mech.*, Vol. 2, 1966, pp. 614-627.

34. J. Pilling and N. Ridley, *Acta Metall.*, Vol. 34, 1986, pp. 669-679.

35. F. A. McClintock, *J. Appl. Mech., Trans. ASME*, Vol. 90, 1969, pp. 363-371.

36. C.A. Berg, in *Proc. 4th US Natl Cong. Appl. Mech.*, ASME, Mew York, Vol. 2, 1962, pp. 855-880.

37. W.M. Garrison and N.R. Moody, *J. Phys. Chem. Solids*, Vol. 48, 1987, pp. 1035-1074

38. P.D. Nicolaou, A.K. Ghosh, and S.L. Semiatin, *Metall. Mater. Trans. A*, Vol. 35A, 2004, pp. 2187-2190.

39. P.D. Nicolaou, R.L. Goetz, and S.L. Semiatin, *Metall. Mater. Trans. A*, Vol. 35A, 2004, pp. 655-663.

40. D.H. Bae, A.K. Ghosh, and J.R. Bradley: *Metall. Mater. Trans. A*, 2003, vol. 34A, pp. 2449-2463.

41. P.D. Nicolaou, J.D. Miller, and S.L. Semiatin, *Metall. Mater. Trans. A*, Vol. 36A, 2005, pp. 3461-3470.

42. T.R. Bieler, P.D. Nicolaou, and S.L. Semiatin, *Metall. Mater. Trans. A*, Vol. 36A, 2005, pp. 129-140.

43. P.D. Nicolaou and S.L. Semiatin, *Metall. Mater. Trans. A*, Vol. 7A, 2006, pp. 1567-1574.

44. S.L. Semiatin, F. Montheillet, G. Shen, and J.J. Jonas, *Metall. Mater. Trans. A*, Vol. 33A, 2002, pp. 2719-2727.

45. J.J. Blandin, B. Hong, A. Varloteaux, M. Suery, and D. L'Esperance,. Acta Mater., Vol. 66, 1996, pp. 2317-2326.

46. M.J. Stowell: in *Superplastic Forming of Structural Alloys*, N.E. Paton and C.H. Hamilton, eds., TMS-AIME, Warrendale, PA, 1982, pp. 321-326.

47. P.D. Nicolaou and S.L. Semiatin, *Metall. Mater. Trans. A*, Vol. 35A, 2004, pp. 1141-1149.

48. J. Pilling, *Mater. Sci. Techn.*, Vol. 1, 1985, pp. 461-466.

49. C.F. Martin, C. Josserond, L. Salvo, J.J. Blandin, P. Cloetens, and E. Boller, *Scripta Mater.*, Vol. 42, 2000, pp. 375-381.

50. P.D. Nicolaou and S.L. Semiatin, *Metall. Mater. Trans.A*, Vol. 37A, 2006, pp. 3697-3705

51. P.D. Nicolaou, R.L. Goetz, and S.L. Semiatin, *Metall. Mater. Trans.A*, Vol. 39A, 2008, pp. 659-665.

52. D.A. Woodford, *Trans. ASM*, Vol. 26, 1969, pp. 291-293.

53. J.J. Jonas and B. Baudelet, *Acta Metall*., Vol. 25, 1977, pp. 43-50.

54. F.A. Nichols, *Acta Metall.*, Vol. 28, 1980, pp. 663-673.

55. A.K. Ghosh and R.A. Ayres, *Metall. Trans.*, Vol. 7A, 1976, pp. 1589-1591.

56. J. Lian and M. Suery, *Mater. Sci. Techn.*, Vol. 2, 1986, pp. 1093-1098.

57. D.-J Zhou, J. Lian, and M. Suery, *Mater. Sci. Techn*., Vol. 4, 1988, pp. 348-353.

58. M. Zaki, *Metall. Mater. Trans. A*, Vol. 27A, 1996, pp. 1043-1046.

59. C.M. Lombard, R.L. Goetz, and S.L. Semiatin, *Metall. Trans. A*, Vol. 24A, 1993, pp. 2039-2047.

60. P.D. Nicolaou, S.L. Semiatin, and C.M. Lombard, *Metall. Mater. Trans. A*, Vol. 27A, 1996, pp. 3112-3119.

61. P.W. Bridgman, *Studies in Large Plastic Flow and Fracture*, McGraw-Hill, New York, NY, 1952.

62. S.L. Semiatin, R.E. Dutton, and S. Shamasundar, *Processing and Fabrication of Advanced Materials IV*, T.S. Srivatsan and J.J. Moore, eds., TMS, Warrendale, PA, 1996, pp. 39–52.

63. P.D. Nicolaou and S.L. Semiatin, *Metall. Mater. Trans. A.*, Vol. 28A, 1997, pp. 885–893.

64. C.M. Lombard, *Superplasticity in Near-Gamma Titanium Aluminides*, Ph.D. Thesis, University of Michigan, Ann Arbor, 2001.

List of Symbols

a, size of major axis of an elliptical cavity
A_o , area of the nominally uniform slice of the specimen
A_{lb}, load bearing area
A_m, macroscopic area of a tension specimen
b, size of minor axis of an elliptical cavity
γ, surface energy of the cavity
γ_p surface energy of a particle
γ_i surface energy of the particle-matrix interface
C_v, cavity volume fraction
C_{vo}, initial cavity volume fraction
D, diffusion coefficient
δ, grain boundary thickness
δ_{ij} , Kronecker delta
$\bar{\varepsilon}$, effective strain
$\dot{\bar{\varepsilon}}$, effective strain rate
ε_o , strain at which a cavity becomes stable
ε, axial strain
$\dot{\varepsilon}_1, \dot{\varepsilon}_2, \dot{\varepsilon}_3$, strain rate along the principal directions 1, 2, 3
$\dot{\varepsilon}_{ij}$,strain rate tensor
ε_N, axial strain at the neck of a specimen
ε_i , strain in the defect portion of the specimen
ε_u ,strain in the uniform region of the specimen
f_h, volume fraction of hard phase
ϕ, stress intensification factor
F, size of initial geometric defect (taper)
F_T, stress triaxiality factor
η, individual cavity-growth rate parameter in uniaxial tension
η_{APP} , apparent cavity growth rate
η^{ts}, individual cavity-growth rate parameter in complex stress state
η_i, cavity growth rate along principal direction “i”
k, Boltzmann’s constant
K, strength coefficient
$k_{D,}$ constant dependent on the geometry of the deformation
L_i, cavity section along principal direction “i”
λ, cavity spacing
m, strain rate sensitivity
M, Taylor factor
M_h, Taylor factor of hard phase
M_s, Taylor factor of soft phase
n, stress exponent
P, applied hydrostatic pressure

r_c, critical cavity radius
r, cavity radius
r_o , radius at which a cavity becomes stable
R, average of the three semi-axes of the cavity

$\bar{r}$, average cavity radius
ρ, relative density
U , profile radius at the neck of a tension specimen
W, half diameter or width of a tension speciment
σ, external normal stress
$\bar{\sigma}_h$, effective stress
$\bar{\sigma}_s$, effective stress of soft phase
$\bar{\sigma}$, effective stress of hard phase
σ_M, mean stress
σ_z, principal stress along the longitudinal direction
σ_r, principal stress along the radial direction
σ_θ, principal stress along the hoop direction
σ_z^{mac}, macroscopic longitudinal stress
σ_r^{mac}, macroscopic radial stress
σ_θ^{mac}, macroscopic hoop stress
$\sigma_{ij}^{'}$, deviatoric stress tensor
s, center-to-center cavity spacing
V, cavity volume
V_o , volume at which a cavity becomes stable
Ω, atomic volume

Figure Captions

Figure 1. Cavitation observations for Ti-6Al-4V with a colony-alpha microstructure: (a) Optical micrograph and (b) SEM micrograph.

Figure 2. Schematic plot of the dependence of the cavity-growth rate on cavity radius for different rate-controlling mechanisms [19].

Figure 3. Measured cavity volume fraction as a function of axial strain from tension testing of a gamma titanium aluminide alloy. The test temperature was 1000°C and the strain rate was 10^{-4} s^{-1} [18].

Figure 4. Simulation results for the ratio of the apparent to individual cavity growth rates as a function of the cavity nucleation rate [27].

Figure 5. Dependence of the ratio of the cavity-growth parameter under triaxial and uniaxial states of stress (η^{ts}/η) on the stress triaxiality ($\sigma_M/\bar{\sigma}$). The measurements (shaded area) are compared to various model predictions [38].

Figure 6. Comparison of predictions from Equation (14) of the average cavity size as a function of the stress triaxiality ($\sigma_M/\bar{\sigma}$) with measured cavity sizes (data points) developed during (a) notched-tension testing of Ti-6Al-4V [39] or (b) equibiaxial-tension testing of a fine-grained 5083 modified aluminum alloy [39,40].

Figure 7. Strain and direction dependence of the size of cavities developed during hot torsion testing of Ti-6Al-4V with a colony-alpha microstructure at 815°C and a surface effective strain rate of 0.04 s^{-1} [41].

Figure 8. Self-consistent model predictions of the average strain rates developed in the individual phases of a two-phase (hard (h) and soft (s)) mixture as a function of k_h/k_s, f, and the macroscopic (imposed) strain rate. The m value for both phases was 0.23 [44].

Figure. 9. Comparison of measurements and predictions of the cavity radius as a function of the Taylor-factor ratio M_h/M_s for cavity radii greater than 3 μm. The solid lines represent predictions for f_h = 0.6 for three different ranges of the cavity-growth strain. The local fraction of hard orientations, f_h, increases in the shaded region from 0.4 to 0.8 in the direction shown [42].

Figure 10. Montage of micrographs along the equatorial plane showing the variation of cavitation in the radial direction developed during hot pancake forging of Ti-6Al-4V with a colony-alpha microstructure [43].

Figure 11. Comparison of measurements and model predictions of the variation of the size of the *largest* cavities as a function of the distance from the free surface for a Ti-6Al-4V pancake hot forged to a 50 pct. height reduction

following preheating at 815°C [43]. Cavity-size measurements were from both axial (r-z) and in-plane (r-θ) sections.

Figure 12. Dependence of the critical strain for ligament failure on the center-to-center cavity spacing and the individual cavity growth rate η [47].

Figure 13. Simulation predicions of the average cavity radius for cavities which do not or do coalesce (Equation (23)). The cavity volume fraction is also shown on the graph.

Figure 14. Three-dimensional view of the largest coalesced cavities obtained via x-ray tomography of a sample of aluminum alloy 5083 following deformation in tension at 525°C and 10^{-4} s^{-1} [22].

Figure 15. X-ray tomography measurements of the cavity interlinkage parameter (IP) as a function of cavity volume fraction in a sample of aluminum alloy 5083 following deformation in tension at 525°C and 10^{-4} s^{-1} [49].

Figure 16. Micrographs showing the effect of strain path on cavitation in Ti-6Al-4V samples with a colony-alpha microstructure deformed at 815°C and an effective strain rate of 0.04 s^{-1} via monotonic torsion, reversed torsion, and compression following monotonic torsion [51].

Figure 17a. Comparison of model predictions (lines) and experimental measurements (data points) of the cavity fraction as a function of effective strain during reversed torsion at 815°C of Ti-6Al-4V samples with two different levels of the initial cavity fraction. The model predictions are plotted for two different ratios of the Taylor factor between the hard and the soft colonies (M_h/M_s) [50].

Figure 17b. Comparison of model predictions (lines) and measurements (data points) of the cavity fraction as a function of the macroscopic effective strain during compression of Ti-6Al-4V samples following torsional pre-deformation to a strain level denoted ε_{in}. Prestraining and compression were both conducted at 815°C and an effective strain rate of 0.04 s^{-1} [51].

Figure 18. Micro-specimen geometry utilized in cavitation analysis by Zaki [58].

Figure 19. Discretization of the sheet specimen for the simulation of flow-localization and cavitation during isothermal hot tension testing [60].

Figure 20. Macroscopic model predictions of total elongation as a function of m and η_{APP} for sheet tension testing of samples with a 2-pct. taper and strain-hardening exponent n = 0 [60]. The individual data points represent measurements taken from the literature.

Figure 21. Failure-mode map developed from macroscopic model simulations of the sheet tension test [60]. Model predictions of the failure mode are compared to experimental observations (data points).

Figure 22. Micrographs of (a) an orthorhombic titanium aluminide alloy which failed in tension by flow localization [63] and (b) a near-gamma titanium aluminide alloy which failed in tension by fracture (cavitation) [64].

Figure 23. Hybrid (macro-micro) and macroscopic model predictions of engineering stress-strain curves for m = 3, N = 100 cav/mm^2, and various values of η [47].

(a)

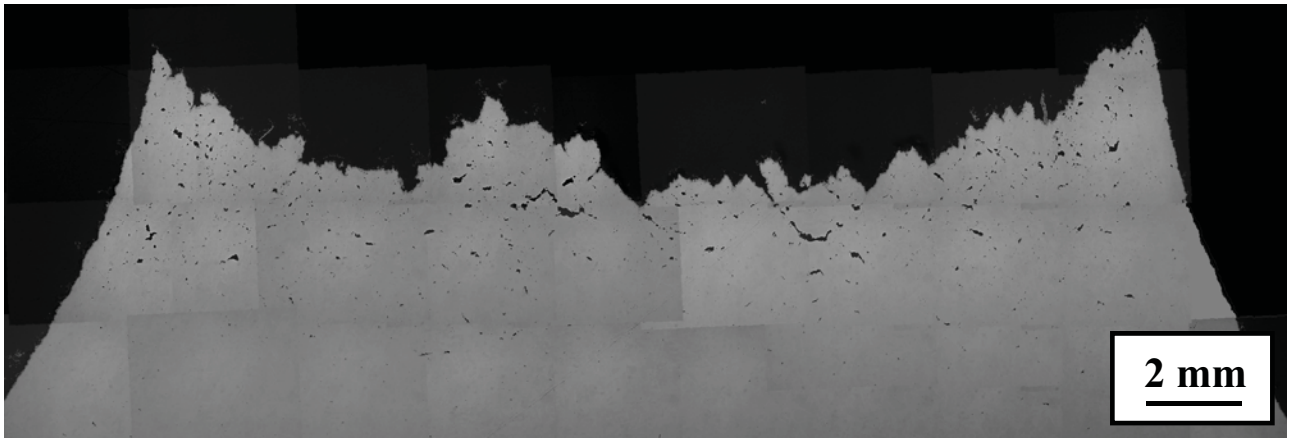

(b)

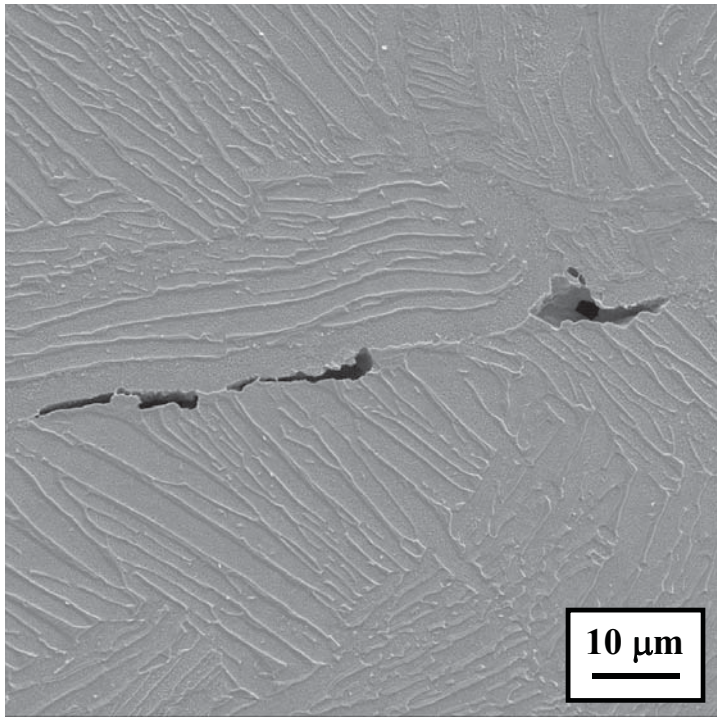

Figure 1. Cavitation observations for Ti-6Al-4V with a colony-alpha microstructure: (a) Optical micrograph and (b) SEM micrograph.

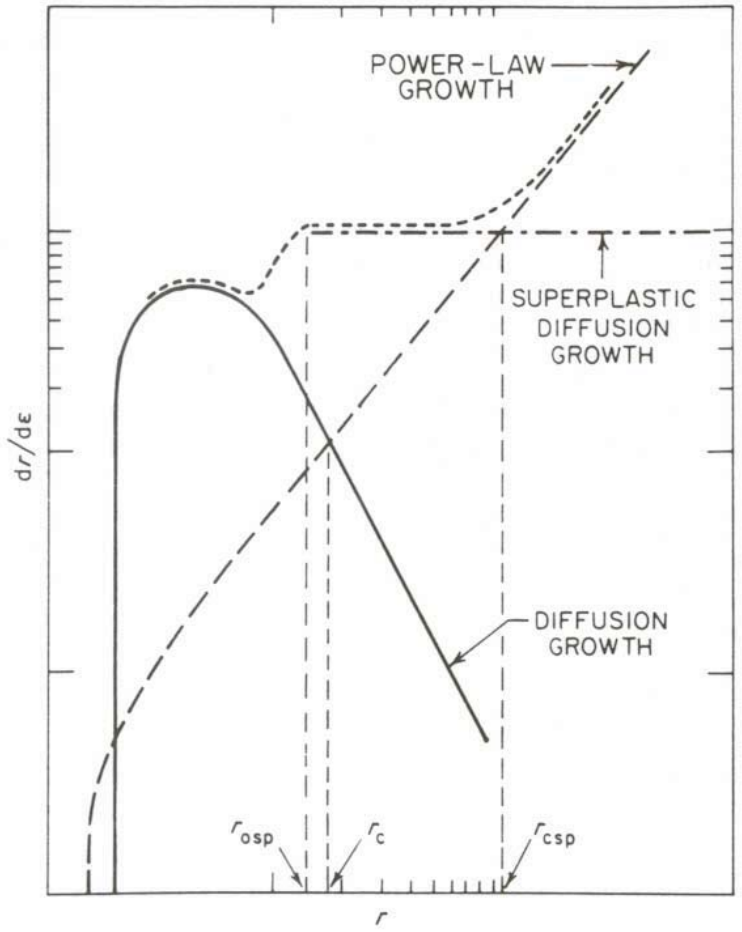

Figure 2. Schematic plot of the dependence of the cavity-growth rate on cavity radius for different rate-controlling mechanisms [19].

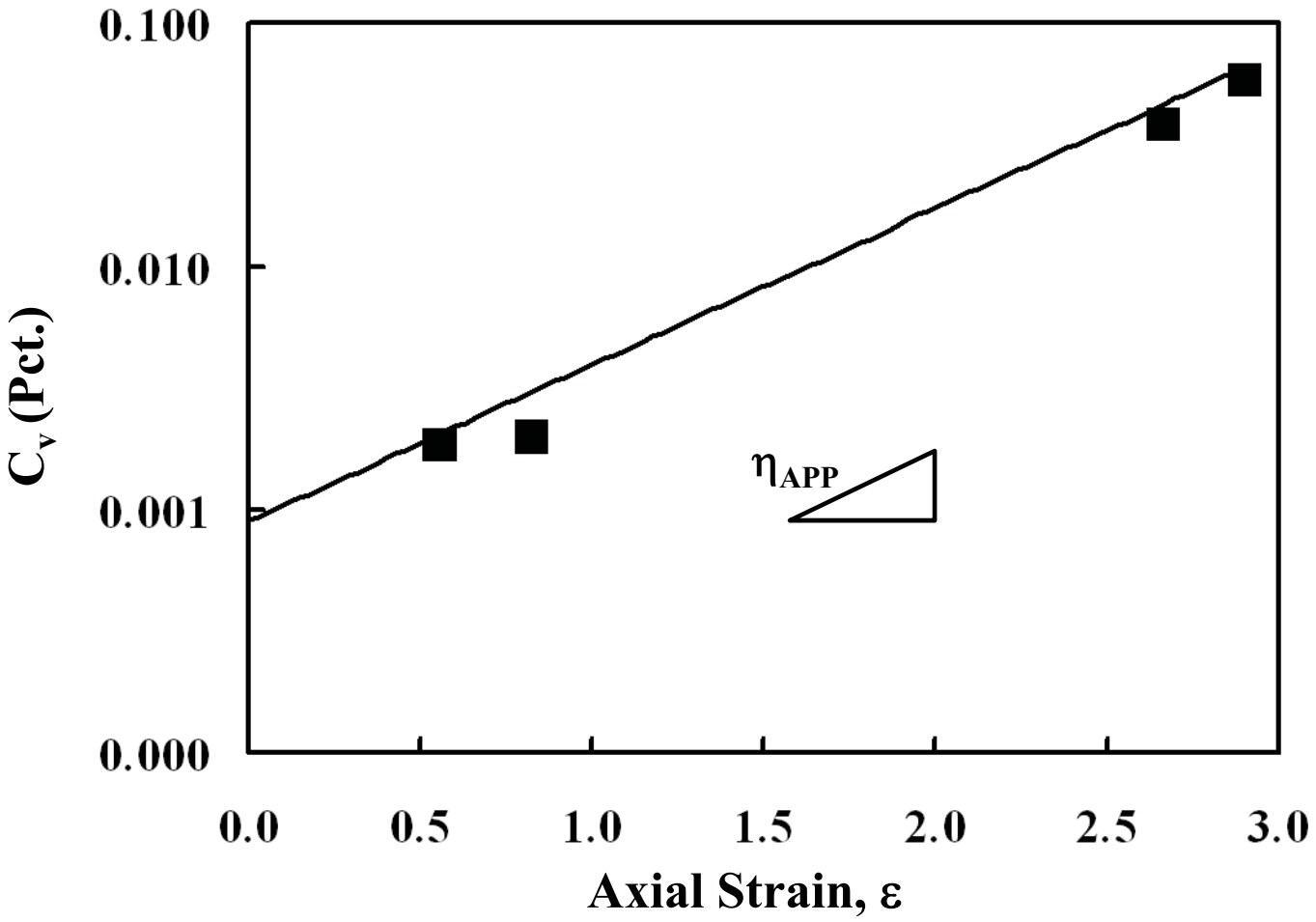

Figure 3. Measured cavity volume fraction as a function of axial strain from tension testing of a gamma titanium aluminide alloy. The test temperature was 1000°C and the strain rate was 10^{-4} s^{-1} [18].

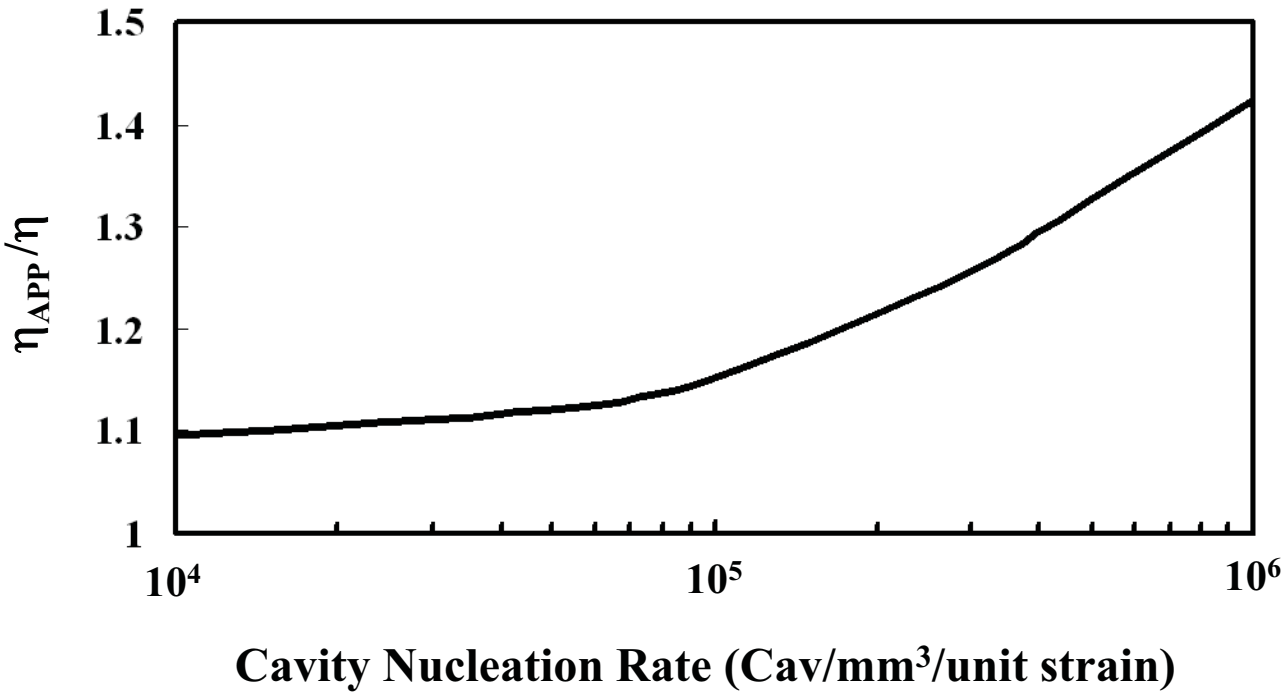

Figure 4. Simulation results for the ratio of the apparent to individual cavity growth rates as a function of the cavity nucleation rate [27].

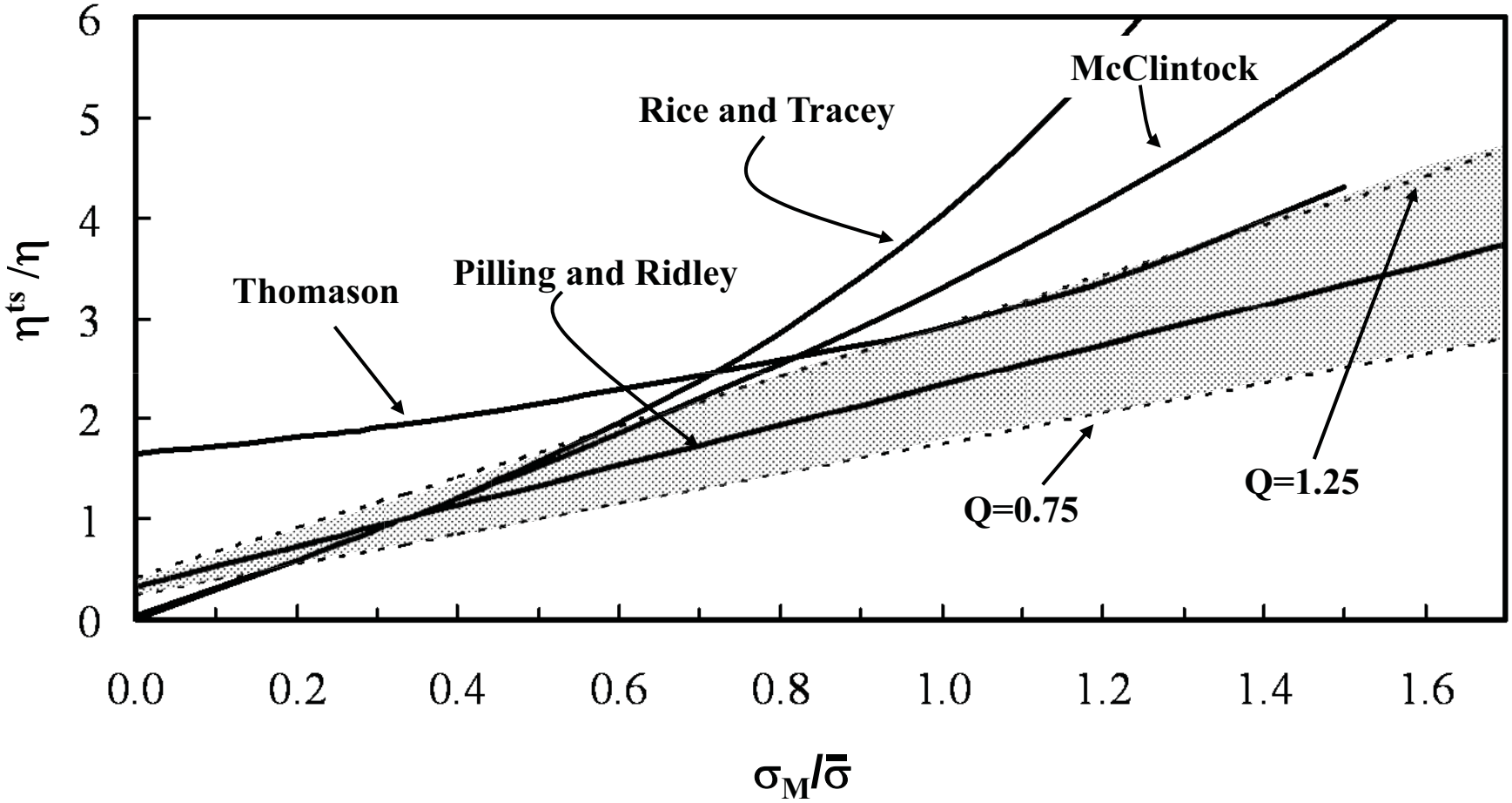

Figure 5. Dependence of the ratio of the cavity-growth parameter under triaxial and uniaxial states of stress (η^{ts}/η) on the stress triaxiality ($\sigma_M/\bar{\sigma}$). The measurements (shaded area) are compared to various model predictions [38].

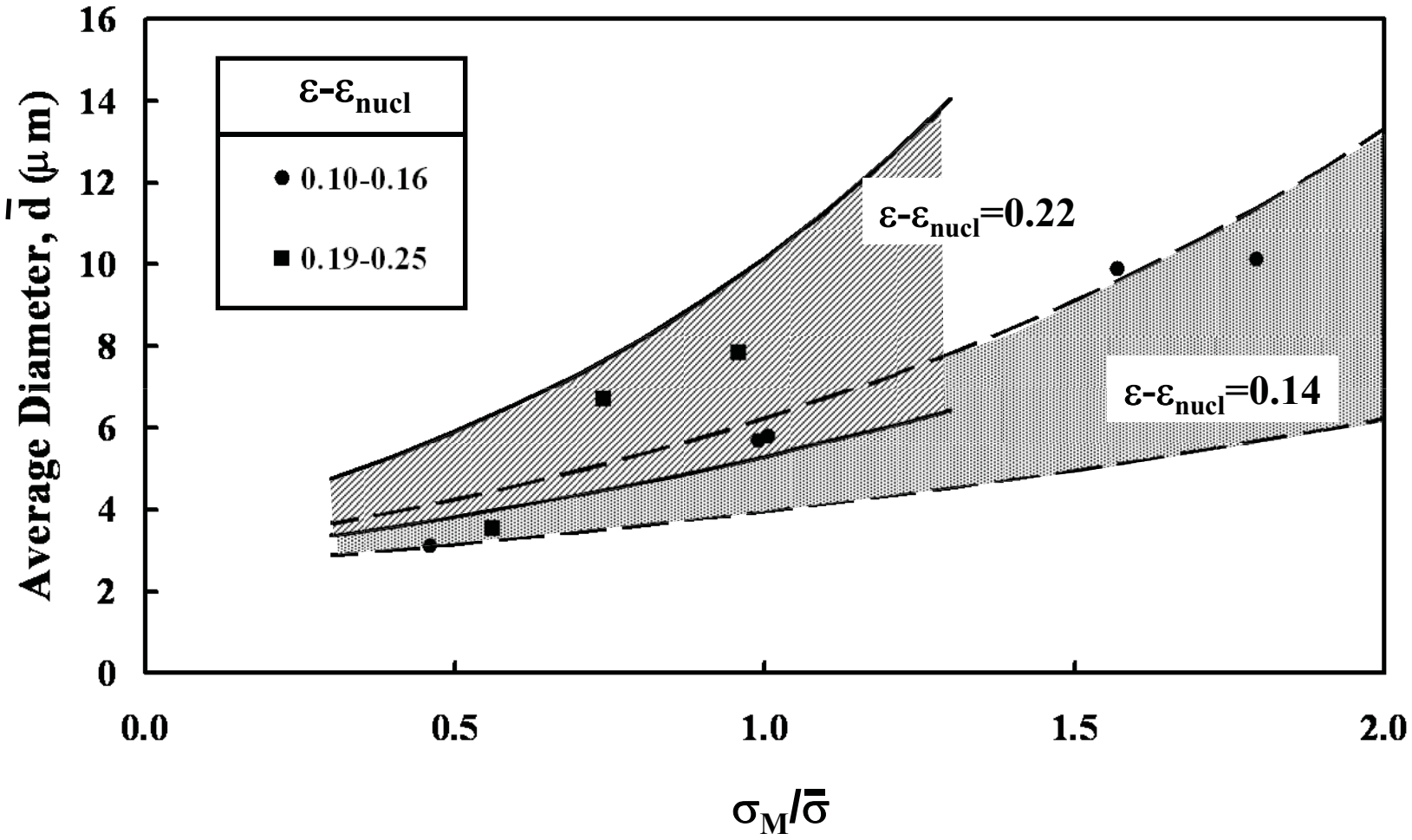
Average Diameter, $\bar{d}$ (μm)
16
14
12
10
8
6
4
2
0
0.0
0.5
1.0
1.5
2.0
$\sigma_M/\bar{\sigma}$
ε-ε$_{nucl}$
0.10-0.16
0.19-0.25
ε-ε$_{nucl}$=0.22
ε-ε$_{nucl}$=0.14

Figure (6a)

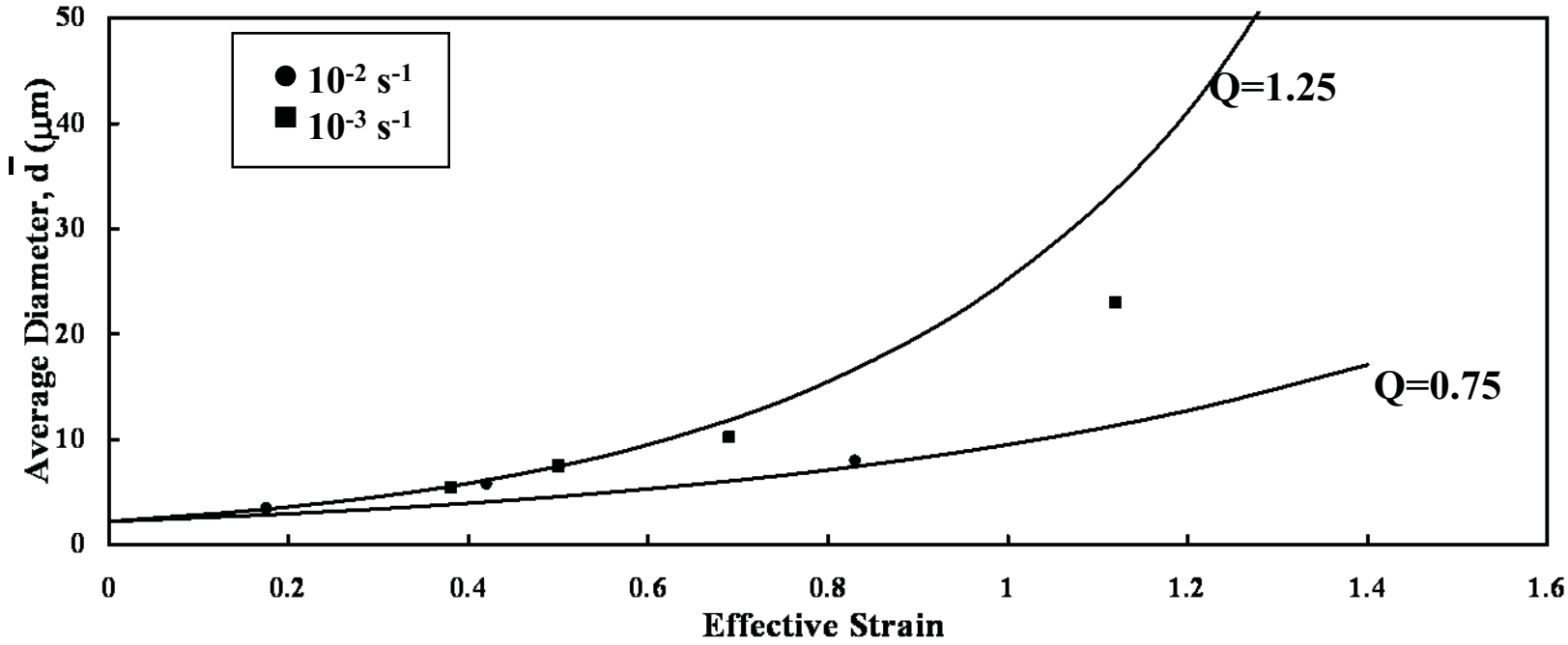

Figure 6. Comparison of predictions from Equation (14) of the average cavity size as a function of the stress triaxiality ($\sigma_M/\bar{\sigma}$) with measured cavity sizes (data points) developed during (a) notched-tension testing of Ti-6Al-4V [39] or (b) equibiaxial-tension testing of a fine-grained 5083 modified aluminum alloy [39,40].

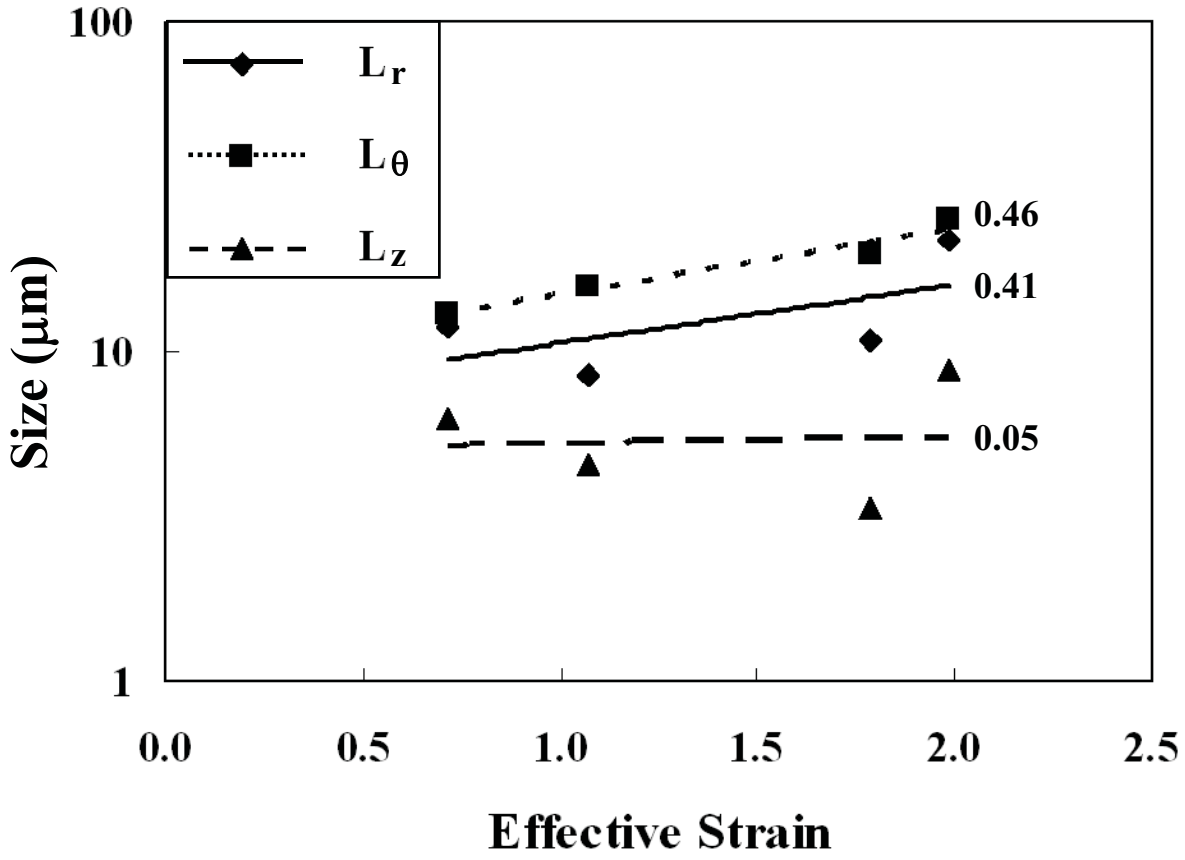

Figure 7. Strain and direction dependence of the size of cavities developed during hot torsion testing of Ti-6Al-4V with a colony-alpha microstructure at 815°C and a surface effective strain rate of 0.04 s^{-1} [41].

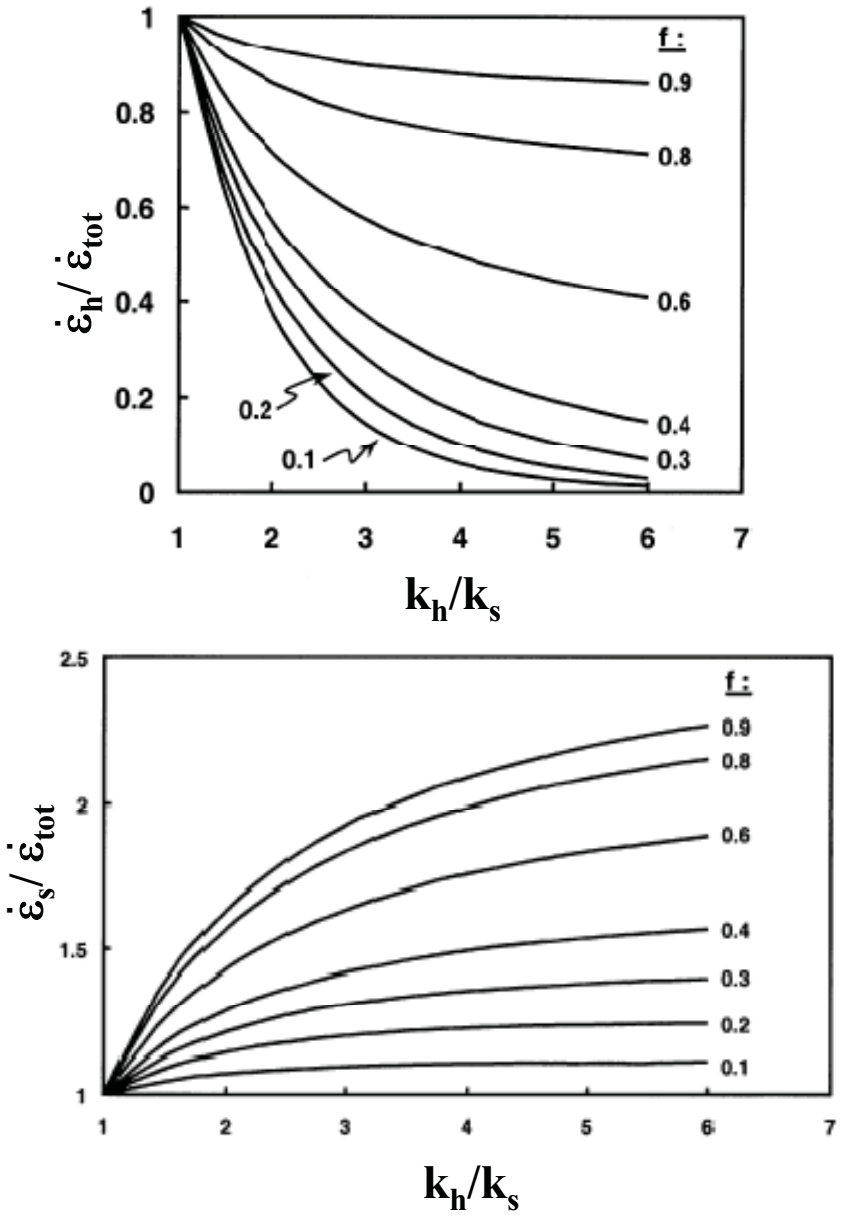

Figure 8. Self-consistent model predictions of the average strain rates developed in the individual phases of a two-phase (hard (h) and soft (s)) mixture as a function of k_h/k_s, f, and the macroscopic (imposed) strain rate. The m value for both phases was 0.23 [44].

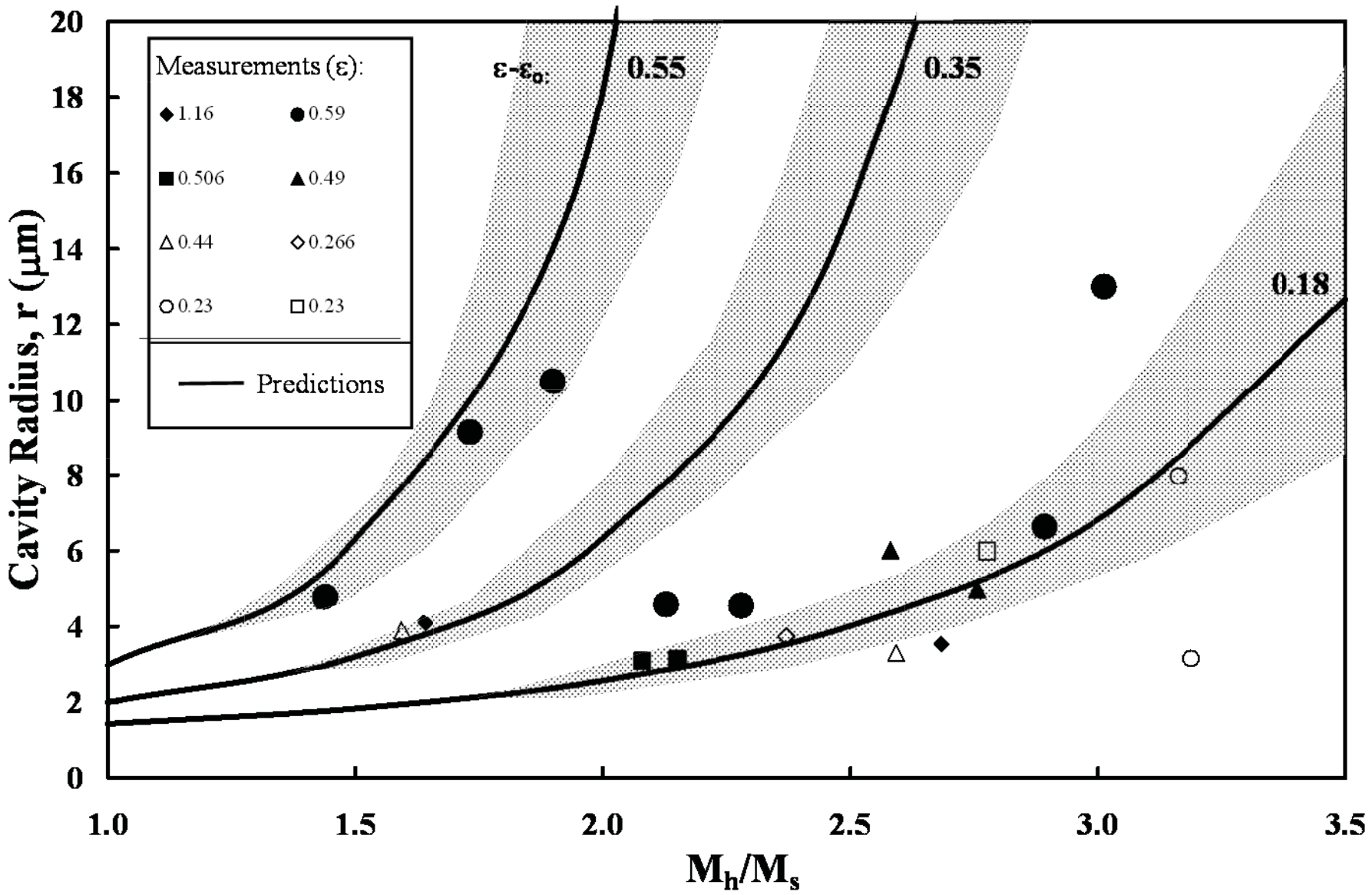

Figure. 9. Comparison of measurements and predictions of the cavity radius as a function of the Taylor-factor ratio M_h/M_s for cavity radii greater than 3 μm. The solid lines represent predictions for $f_h = 0.6$ for three different ranges of the cavity-growth strain. The local fraction of hard orientations, f_h, increases in the shaded region from 0.4 to 0.8 in the direction shown [42].

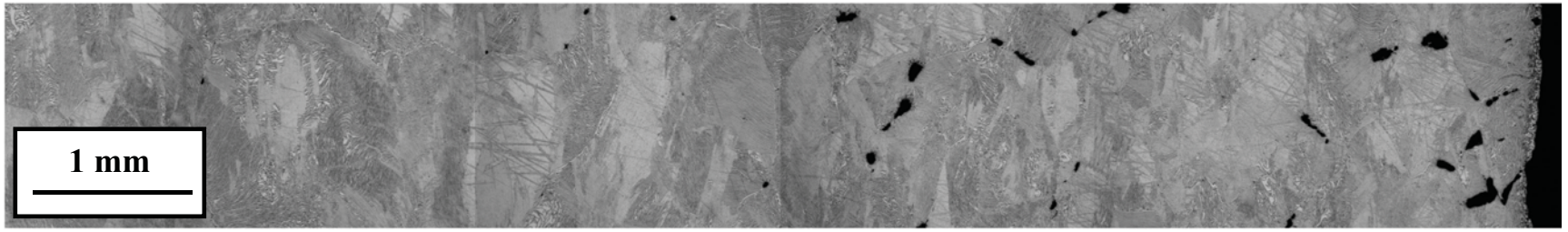

Figure 10. Montage of micrographs along the equatorial plane showing the variation of cavitation in the radial direction developed during hot pancake forging of Ti-6Al-4V with a colony-alpha microstructure [43].

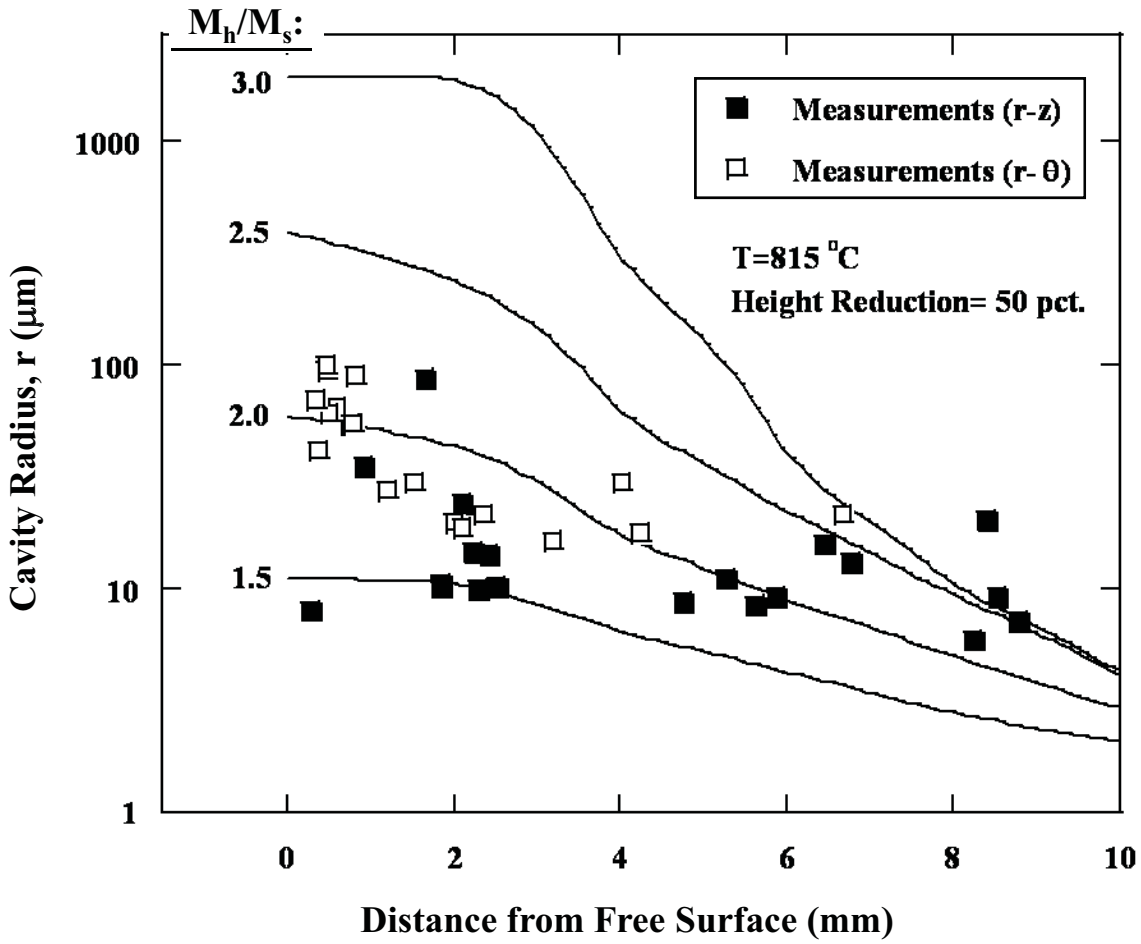

Figure 11. Comparison of measurements and model predictions of the variation of the size of the ***largest*** cavities as a function of the distance from the free surface for a Ti-6Al-4V pancake hot forged to a 50 pct. height reduction following preheating at 815°C [43]. Cavity-size measurements were from both axial (r-z) and in-plane (r-θ) sections.

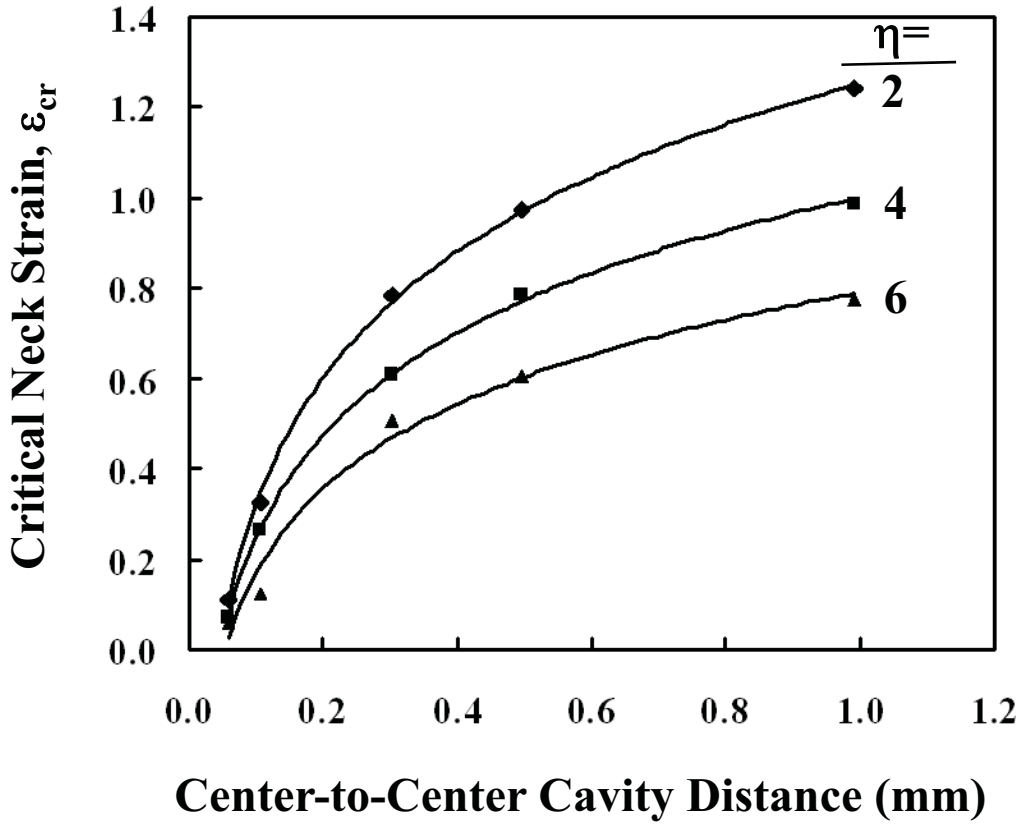

Figure 12. Dependence of the critical strain for ligament failure on the center-to-center cavity spacing and the individual cavity growth rate η [47].

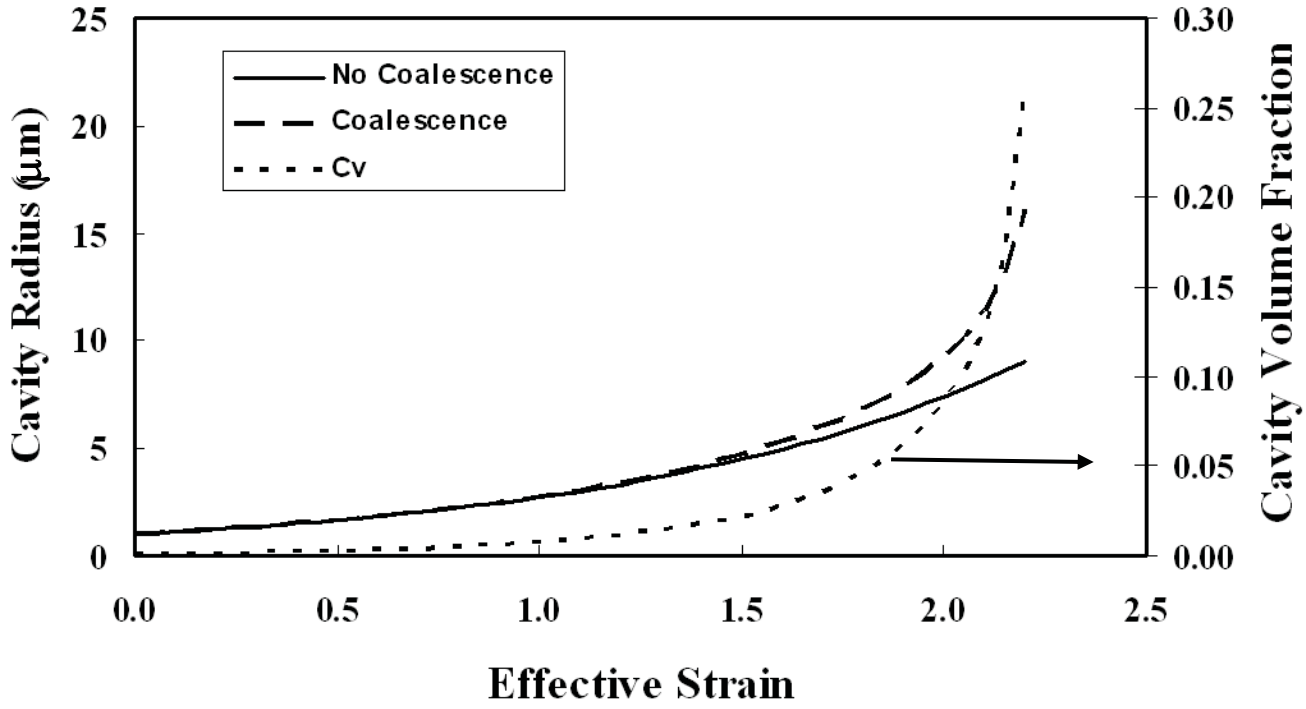

Figure 13. Simulation predicions of the average cavity radius for cavities which do not or do coalesce (Equation (23)). The cavity volume fraction is also shown on the graph.

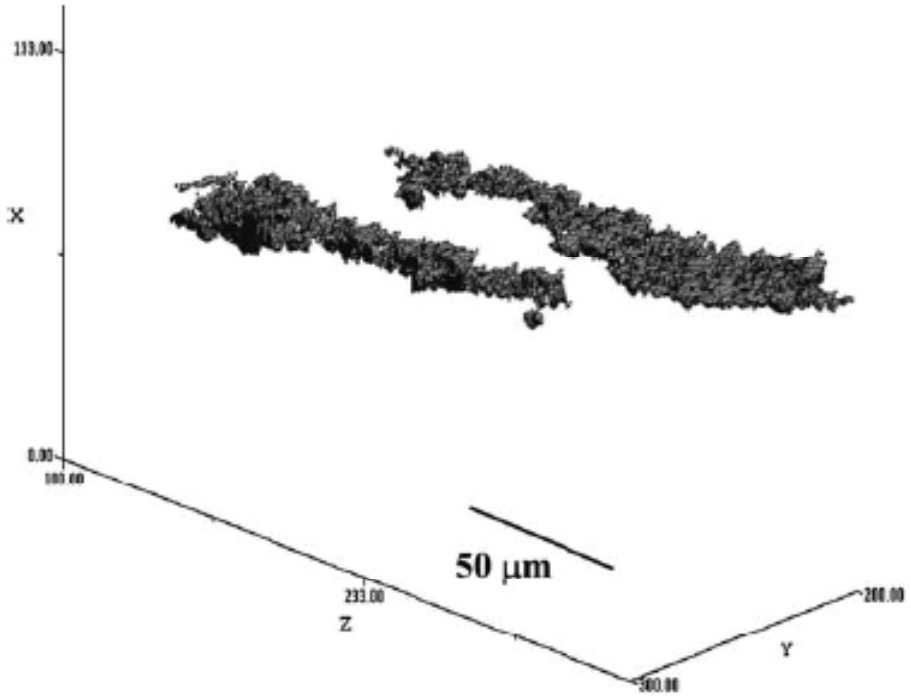

Figure 14. Three-dimensional view of the largest coalesced cavities obtained via x-ray tomography of a sample of aluminum alloy 5083 following deformation in tension at 525°C and 10^{-4} s^{-1} [22].

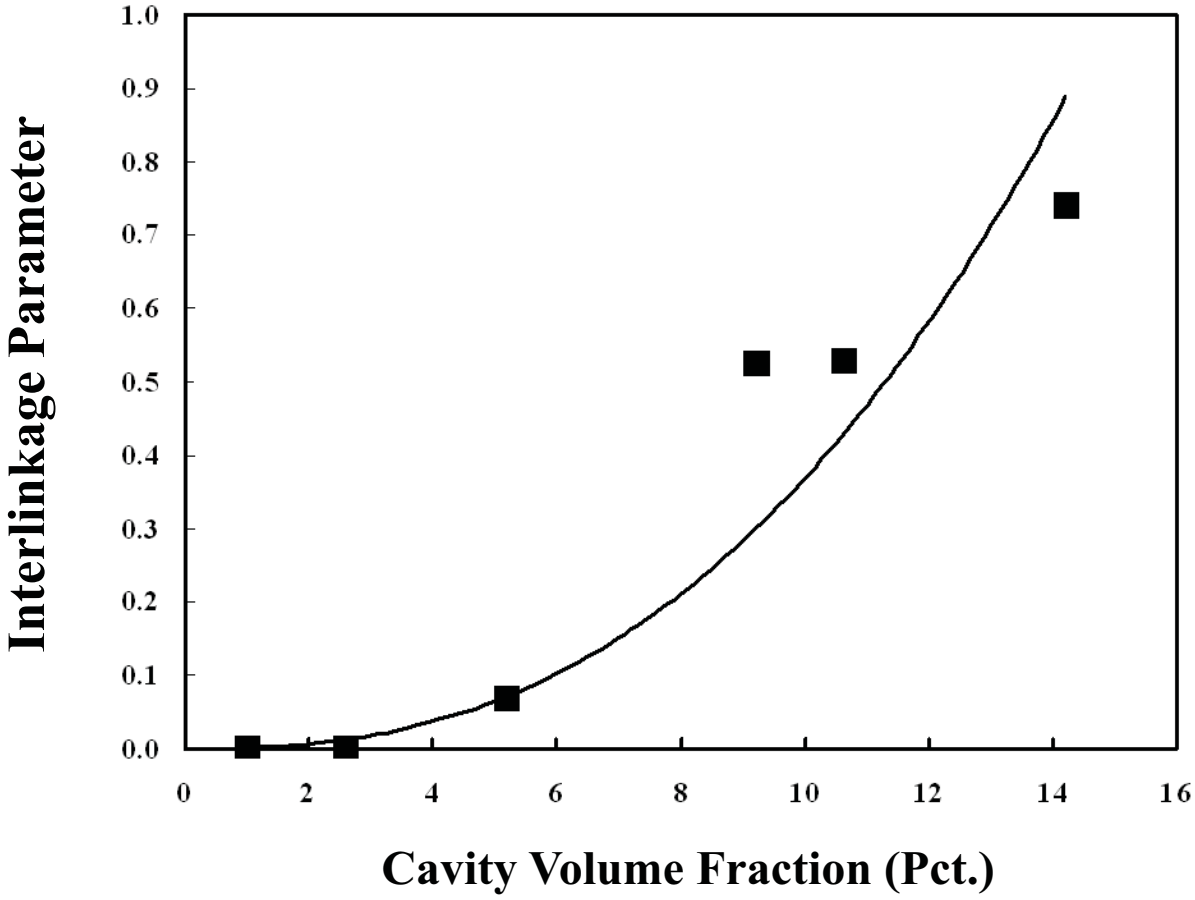

Figure 15. X-ray tomography measurements of the cavity interlinkage parameter (IP) as a function of cavity volume fraction in a sample of aluminum alloy 5083 following deformation in tension at 525°C and 10^{-4} s^{-1} [49].

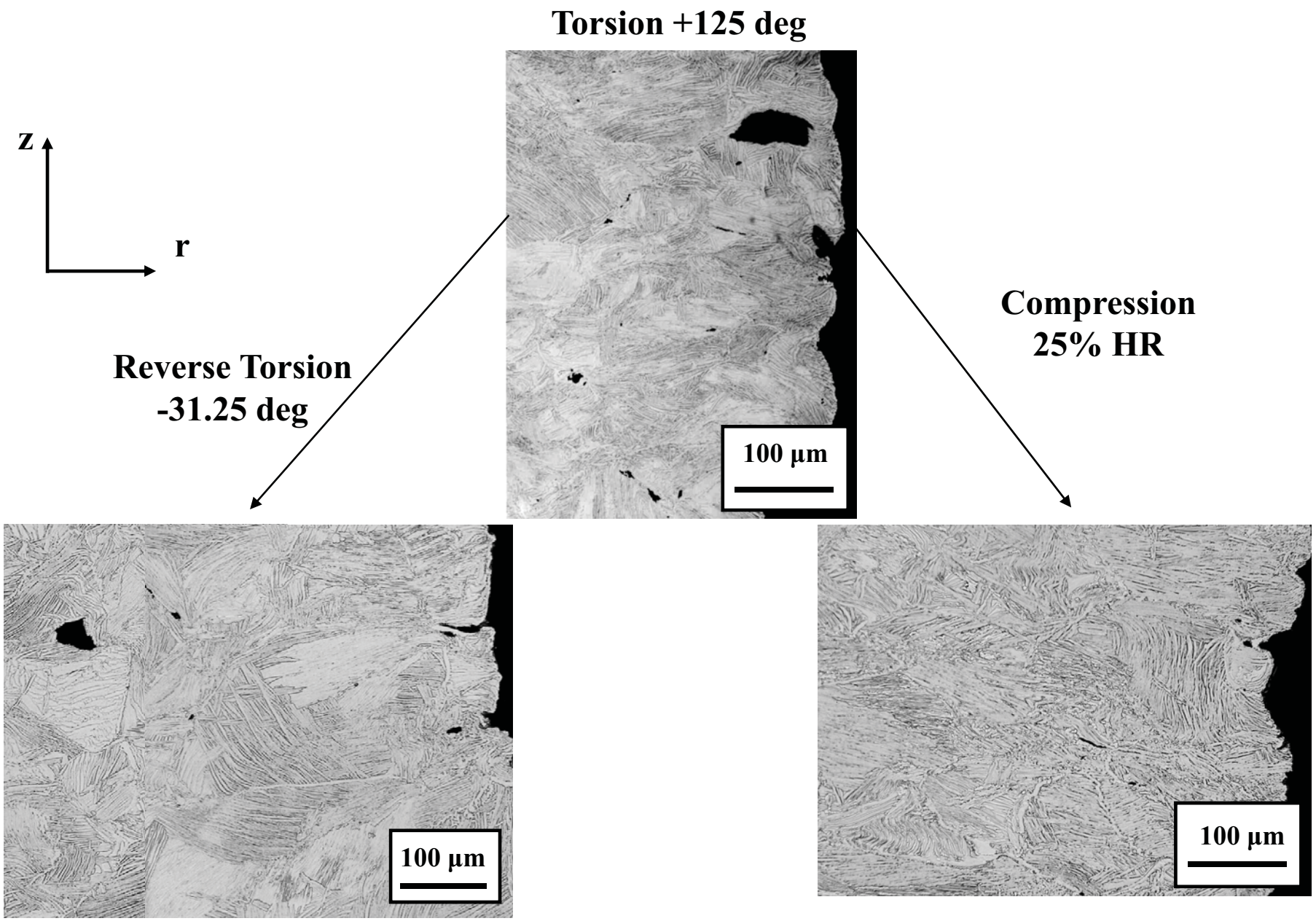

Figure 16. Micrographs showing the effect of strain path on cavitation in Ti-6Al-4V samples with a colony-alpha microstructure deformed at 815°C and an effective strain rate of 0.04 s^{-1} via monotonic torsion, reversed torsion, and compression following monotonic torsion [51].

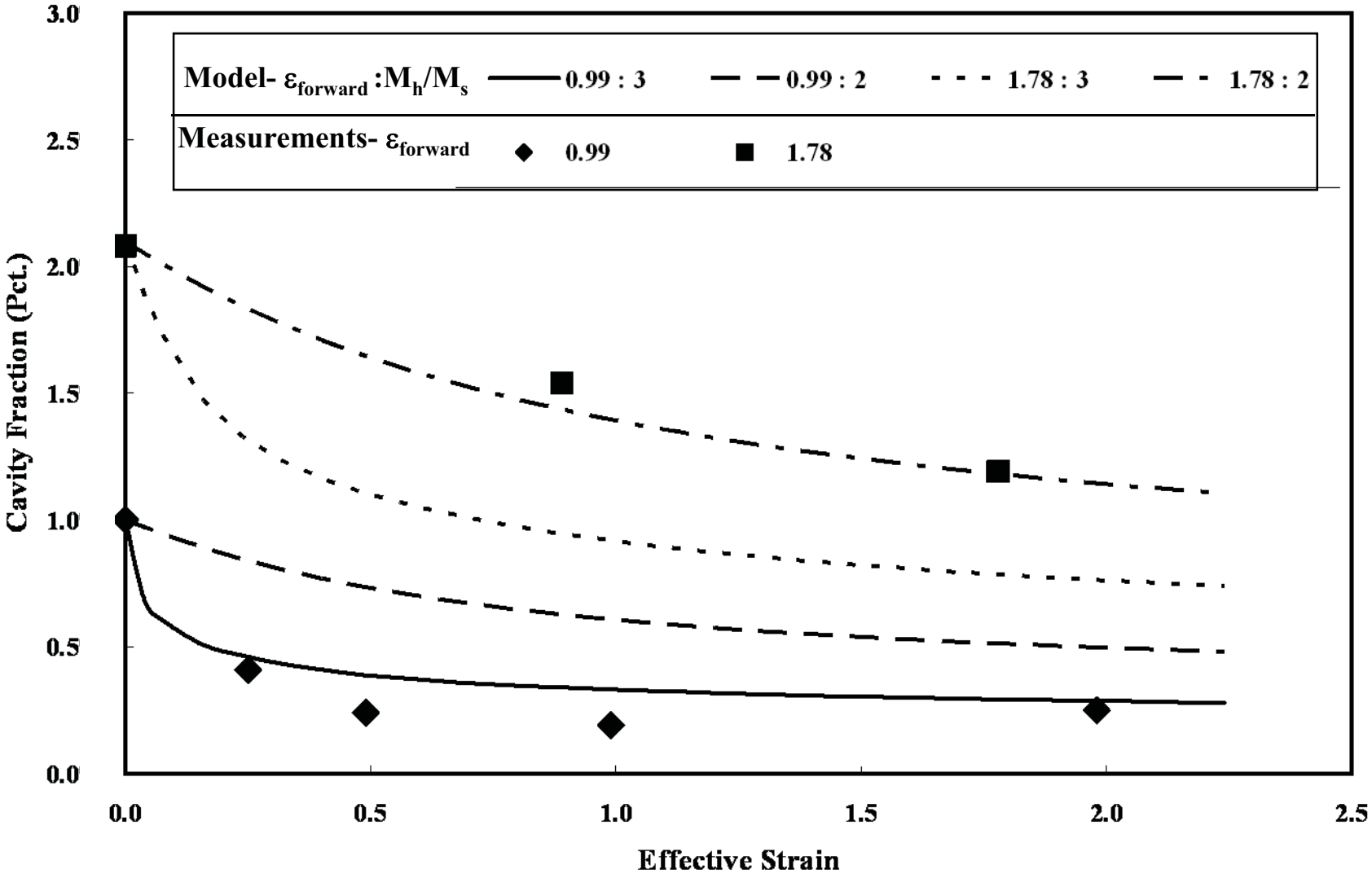

Figure 17a. Comparison of model predictions (lines) and experimental measurements (data points) of the cavity fraction as a function of effective strain during reversed torsion at 815°C of Ti-6Al-4V samples with two different levels of the initial cavity fraction. The model predictions are plotted for two different ratios of the Taylor factor between the hard and the soft colonies (M_h/M_s) [50].

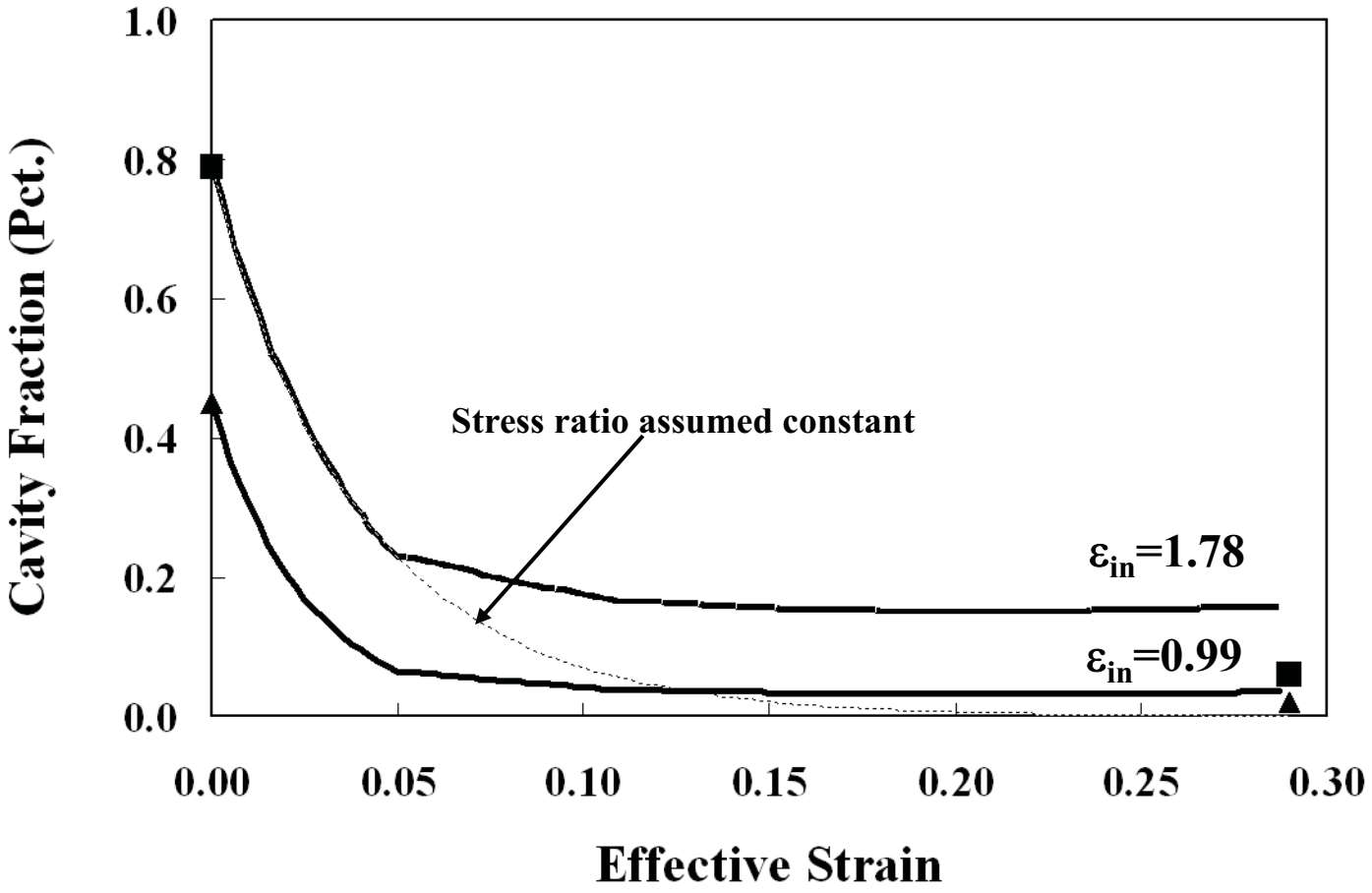

Figure 17b. Comparison of model predictions (lines) and measurements (data points) of the cavity fraction as a function of the macroscopic effective strain during compression of Ti-6Al-4V samples following torsional pre-deformation to a strain level denoted ε_{in}. Prestraining and compression were both conducted at 815°C and an effective strain rate of 0.04 s^{-1} [51].

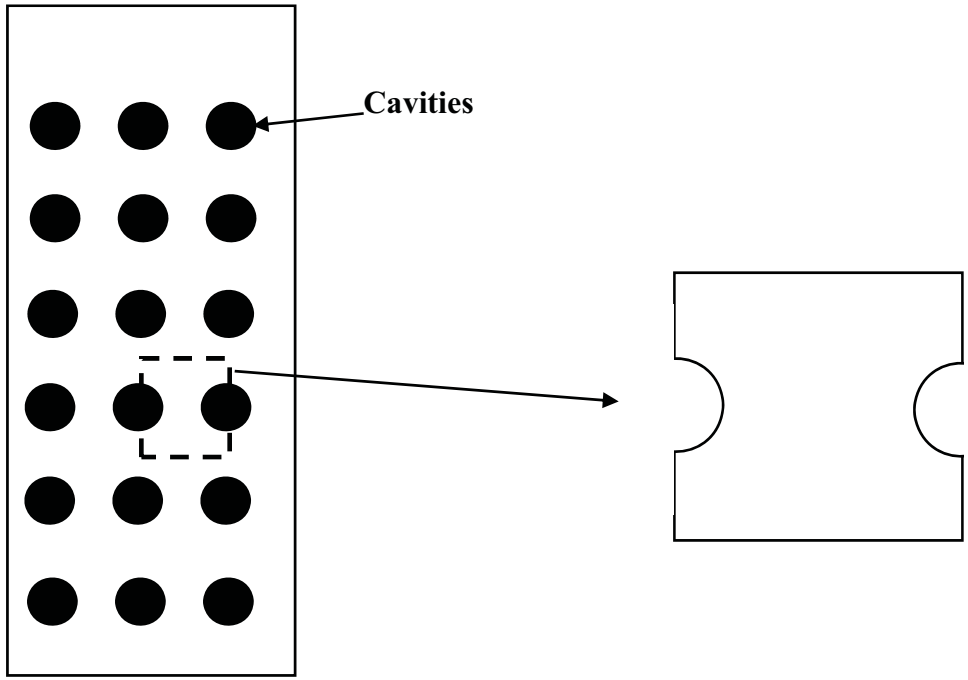

Figure 18. Micro-specimen geometry utilized in cavitation analysis by Zaki [58].

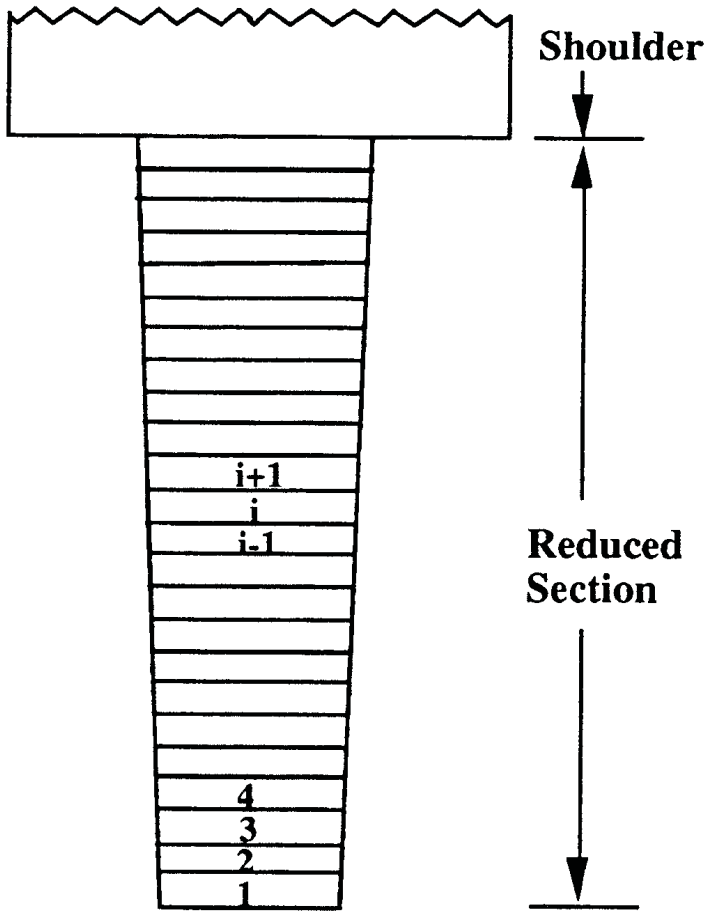

Figure 19. Discretization of the sheet specimen for the simulation of flow-localization and cavitation during isothermal hot tension testing [60].

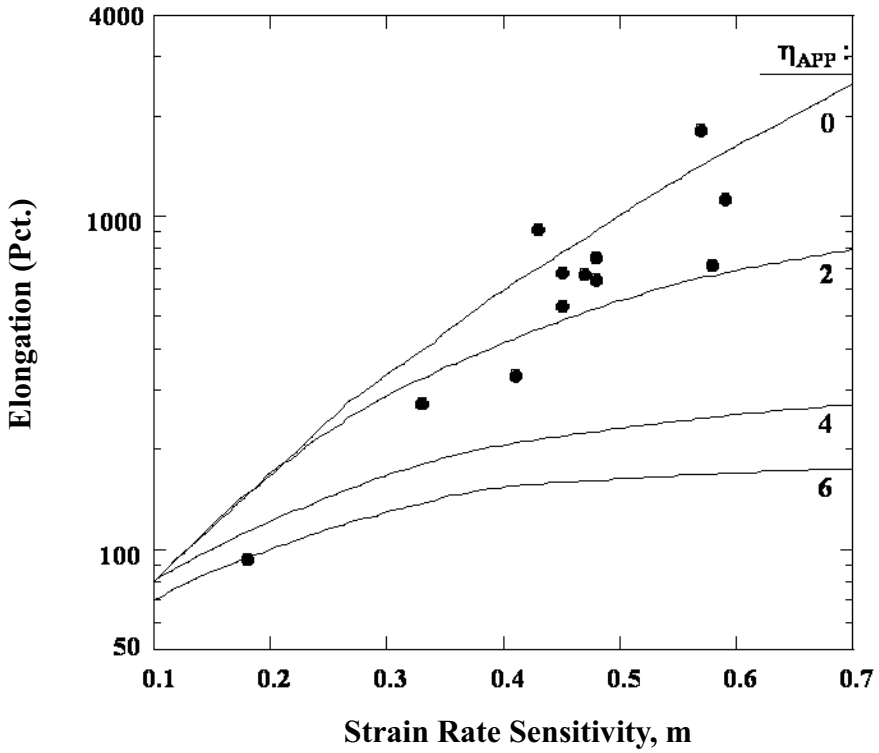

Figure 20. Macroscopic model predictions of total elongation as a function of m and η_{APP} for sheet tension testing of samples with a 2-pct. taper and strain-hardening exponent n = 0 [60]. The individual data points represent measurements taken from the literature.

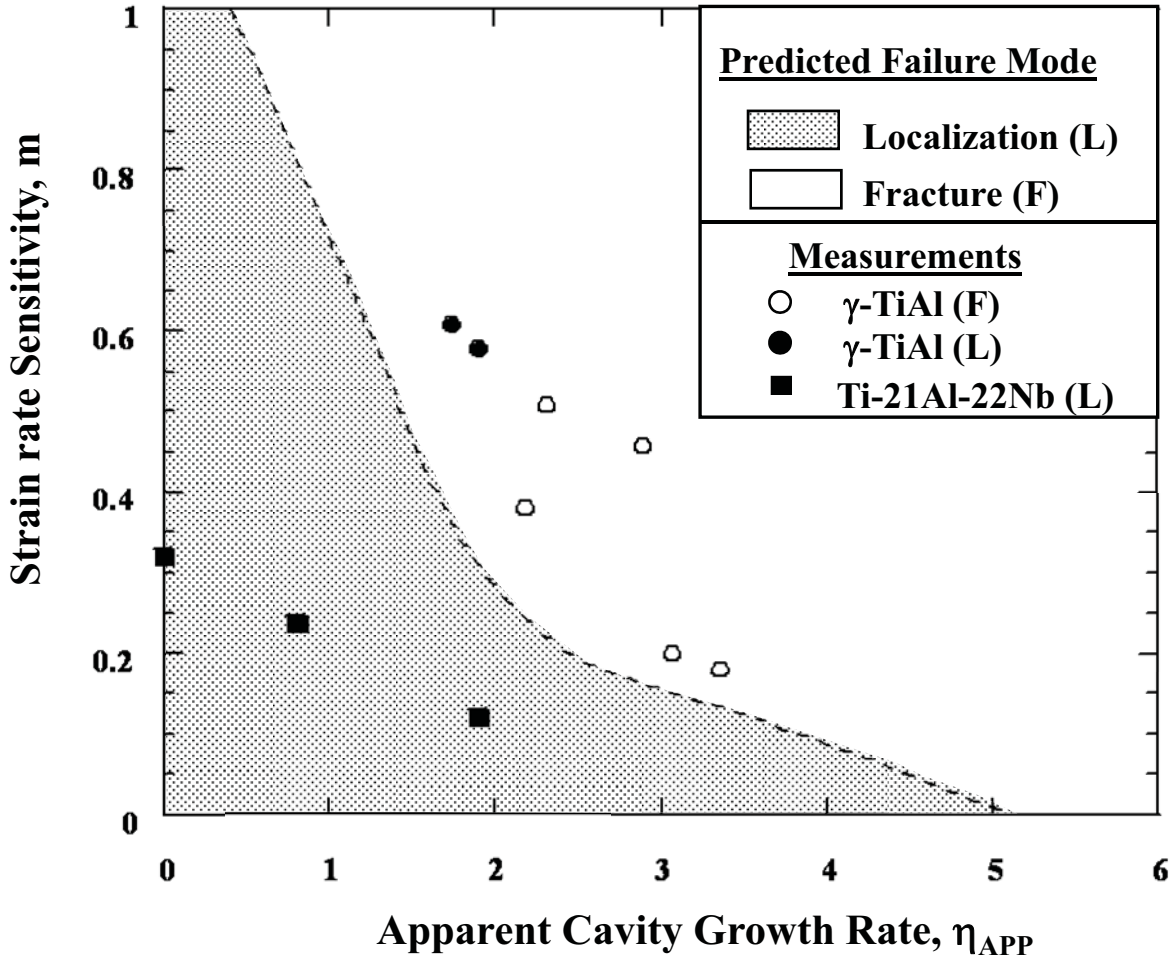

Figure 21. Failure-mode map developed from macroscopic model simulations of the sheet tension test [60]. Model predictions of the failure mode are compared to experimental observations (data points).

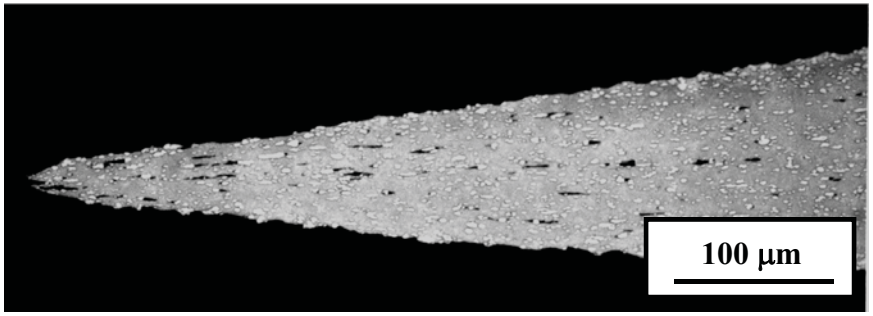

(a)

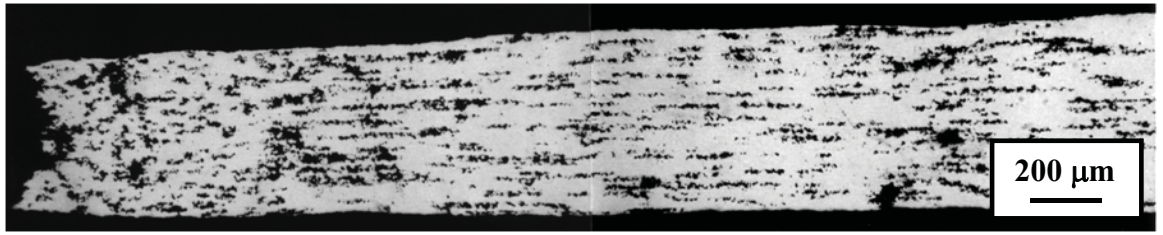

(b)

Figure 22. Micrographs of (a) an orthorhombic titanium aluminide alloy which failed in tension by flow localization [63] and (b) a near-gamma titanium aluminide alloy which failed in tension by fracture (cavitation) [64].

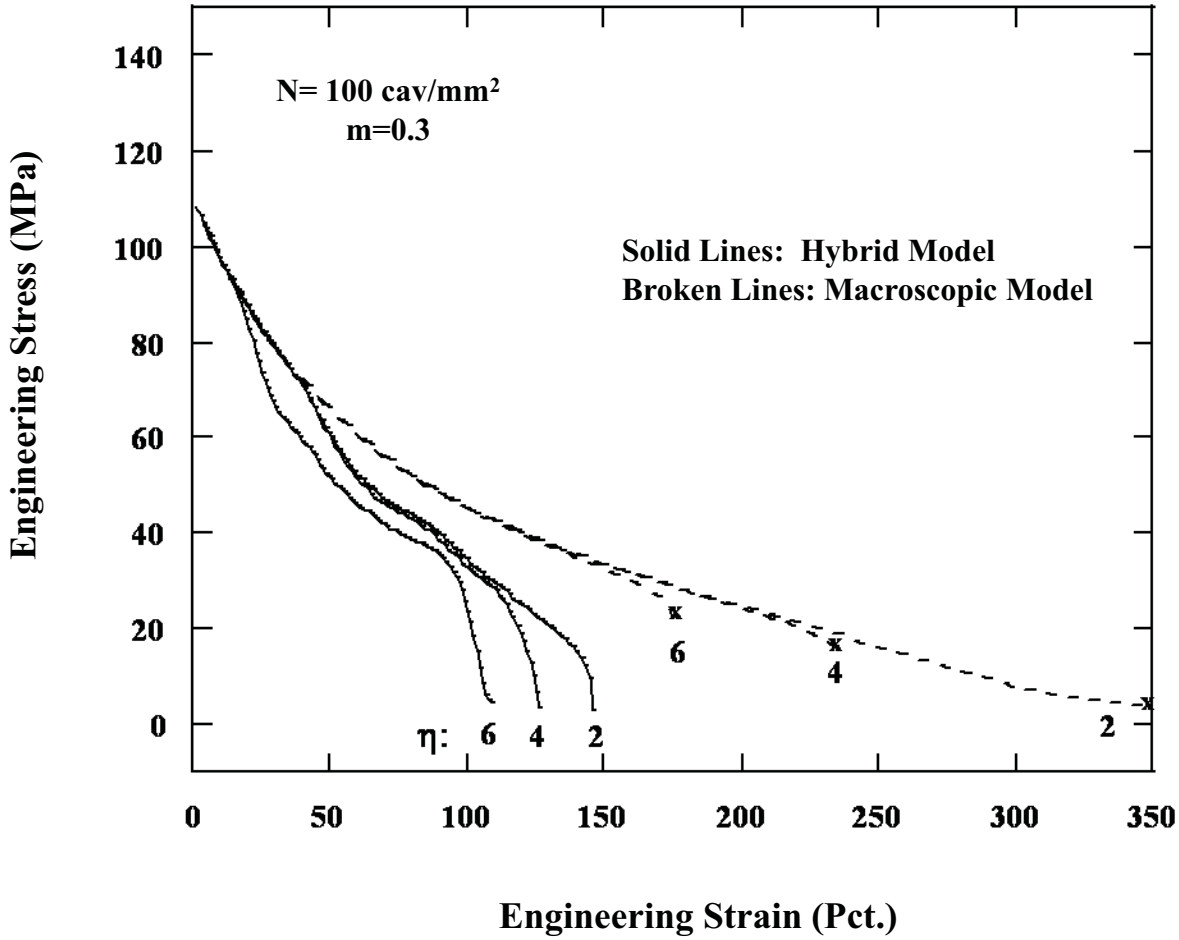

Figure 23. Hybrid (macro-micro) and macroscopic model predictions of engineering stress-strain curves for m = 3, N = 100 cav/mm^2, and various values of η [47].